Photosynthesis versus Exopolymer Degradation in the Formation of Microbialites on the Atoll of Kiritimati, Republic of Kiribati, Central Pacific

Gernot Arp [a] , Gert Helms [a] , Klementyna Karlinska [a] , Gabriela Schumann [a] , Andreas Reimer [a] , Joachim Reitner [a] & Jean Trichet [b]

[a] Geowissenschaftliches Zentrum, Universität Göttingen, Göttingen, Germany

[b] Laboratoire de Géologie de la Matière Organique, Université d'Orléans, Orléans Cedex 2, France

PLEASE SCROLL DOWN FOR ARTICLE

Taylor & Francis
Taylor & Francis Group

Photosynthesis versus Exopolymer Degradation in the Formation of Microbialites on the Atoll of Kiritimati, Republic of Kiribati, Central Pacific

Gernot Arp,[1] Gert Helms,[1] Klementyna Karlinska,[1] Gabriela Schumann,[1] Andreas Reimer,[1] Joachim Reitner,[1] and Jean Trichet[2]

[1]*Geowissenschaftliches Zentrum, Universität Göttingen, Göttingen, Germany*
[2]*Laboratoire de Géologie de la Matière Organique, Université d'Orléans, Orléans Cedex 2, France*

Aragonitic microbialites, characterized by a reticulate fabric, were discovered beneath lacustrine microbial mats on the atoll of Kiritimati, Republic of Kiribati, Central Pacific. The microbial mats, with cyanobacteria as major primary producers, grow in evaporated seawater modified by calcium carbonate and gypsum precipitation and calcium influx via surface and/or groundwaters. Despite the high aragonite supersaturation and a high photosynthetic activity, only minor aragonite precipitates are observed in the top parts of the microbial mats. Instead, major aragonite precipitation takes place in lower mat parts at the transition to the anoxic zone. The prokaryotic community shows a high number of phylotypes closely related to halotolerant taxa and/or taxa with preference to oligotrophic habitats. Soil- and plant- inhabiting bacteria underline a potential surface or subsurface influx from terrestrial areas, while chitinase-producing representatives coincide with the occurrence of insect remains in the mats. Strikingly, many of the clones have their closest relatives in microorganisms either involved in methane production or consumption of methane or methyl compounds. Methanogens, represented by the methylotrophic genus *Methanohalophilus*, appear to be one of the dominant organisms in anaerobic mat parts. All this points to a significant role of methane and methyl components in the carbon cycle of the mats. Nonetheless, thin sections and physicochemical gradients through the mats, as well as the ^{12}C-depleted carbon isotope signatures of carbonates indicate that spherulitic components of the microbialites initiate in the photosynthesis-dominated orange mat top layer, and further grow in the green and purple layer below. Therefore, these spherulites are considered as product of an extraordinary high photosynthesis effect simultaneous to a high inhibition by pristine exopolymers. Then, successive heterotrophic bacterial activity leads to a condensation of the exopolymer framework, and finally to the formation of crevice-like zones of partly degraded exopolymers. Here initiation of horizontal aragonite layers and vertical aragonite sheets of the microbialite occurs, which are considered as a product of high photosynthesis at decreasing degree of inhibition. Finally, at low supersaturation and almost lack of inhibition, syntaxial growth of aragonite crystals at lamellae surfaces leads to thin fibrous aragonite veneers. While sulfate reduction, methylotrophy, methanogenesis and ammonification play an important role in element cycling of the mat, there is currently no evidence for a crucial role of them in CaCO$_3$ precipitation. Instead, photosynthesis and exopolymer degradation sufficiently explain the observed pattern and fabric of microbialite formation.

INTRODUCTION

The formation of microbial carbonates, known from the Archaean to present-day, is driven by a variety of microbial processes, either affecting the ion activity product Ca^{2+} × CO$_3^{2-}$ or kinetics of nucleation processes (for review see Riding 2000; Dupraz et al. 2009). Recent investigations focus on potential impact of anaerobic oxidation of methane or sulphate-reduction and heterotrophic activity on microbialite formation (e.g., Aloisi et al. 2002; Baumgartner et al. 2006), while e.g., photosynthetic CO$_2$-assimilation has long been recognized as potentially

driving microbial CaCO₃ precipitation (von Pia 1934). How-
ever, the complexity of microbial communities and the diffi-
culty in quantifying the various effects make it demanding to
elucidate few key factors that control *de facto* mineral precip-
itation, microbialite fabric formation and distribution. Identi-
fication of such key factors, however, is crucial to derive im-
plications from microbialites for the reconstruction of fossil
environments through Earth History.

One setting of modern microbialite formation is represented
by halite lakes and hypersaline lagoons, i.e., seawater con-
centrated by evaporation. Although the initial idea was that
microbialites growth is favoured here by the lack of biofilm-
grazing metazoa (Garrett 1970), lacking because of high salin-
ities, later suggestions argue that increased calcium carbonate
mineral saturations are the major prerequisite for microbialite
growth (Kempe & Kazmierczak 1990). Apart from that, a high
number of present-day microbialite forming settings is known,
from thermal and karstwater springs to halite lakes, soda lakes,
and marginal marine settings (e.g., Kempe et al. 1991; Reid and
Brown 1991; Winsborough et al. 1994; Jones and Renaut 1996;
Arp et al. 1998, 2010; Laval et al. 2002; Dupraz et al. 2004;
Pentecost 2005; Lim et al. 2009). In these settings, thin biofilms
rather form well-laminated stromatolites, whereas thick micro-
bial mats produce coarse-laminated to highly-porous, irregular
microbialites.

In 2002, we discovered highly-porous reticulate micro-
bialites below thick microbial mats in hypersaline lakes on the
atoll of Kiritimati, Republic of Kiribati, Central Pacific. Previ-
ously, friable patchy CaCO₃ precipitates related to organomin-
eralization have been reported from photosynthesizing thick
microbial mats of brackish marine lakes, which are numerous
on this atoll (Defarge et al. 1996; Trichet et al. 2001). The
hypersaline lakes are filled with evaporated seawater, with no
siliciclastic influx, but temporal surface recharge with mete-
oric freshwater. In this paper, we describe the environmental
setting, prokaryotic composition and structure of the microbial
mats as well as fabric and geochemistry of their microbialites.
Finally, we assess the relative importance of exopolymer degra-
dation, sulfate reduction, methanogenesis and methylotrophy,
and photosynthetic CO₂ assimilation in the formation of the
microbialites.

LOCATION AND ENVIRONMENTAL SETTING

The atoll of Kiritimati (formerly Christmas Island), dis-
covered by Captain James Cook on December 24 in 1777
(Woodroffe and McLean 1998), is part of the Northern Line Is-
lands of Republic of Kiribati (Central Pacific), located close to
the Equator (1°55′ N, 157°25′ W) in the equatorial dry belt (Va-
lencia 1977; Government of Kiribati 1993). The atoll is 41 km
long from NW to SE and 25 km from N to S coast at the west-
ern end (Figure 1). It is the largest atoll of Earth as defined
by land area (ca. 360 km²; Valencia 1977; 321 km² Woodroffe

& McLean 1998). The region shows a uniformly dry climate
(Valencia 1977), however, affected by El Niño Southern Os-
cillation (ENSO), causing heavy rainfall approximately every
4 years (Falkland and Woodroffe 1997; Trichet et al. 2001;
Figure 2).

Numerous lakes (ca. 500; Trichet et al. 2001), with salinities
ranging from nearly fresh to hypersaline (Saenger et al. 2006),
occupy the inner parts of the atoll (Figure 1). Most of them
harbour microbial mats. The lakes are separated by a net-like
system of subfossil ridges of reef carbonates (4500 to 1500 ra-
diocarbon years BP; Woodroffe and McLean 1998). Below that,
reef carbonates penetrated by drillings are of Mid-Pleistocene
age or older (Woodroffe and McLean 1998). Gravity and mag-
netic surveys suggest that the volcanic basement is at shallow
depths at the northern end of the island (Northrop 1962). There
is no source of siliciclastic or volcanoclastic influx on the island.

The distinct morphology of the atoll, with a lagoon in the
west, reticulate ridges with lakes in the centre and a largely dry
eastern part (Figure 1), reflects at least partly a drop in sealevel
after a Mid-Holocene highstand (Valencia 1977, Woodroffe and
McLean 1998) and possibly a northwestward tilting of the atoll
(Valencia 1977). However, the channel connecting the lagoon
with ocean may rather reflect a leak point (Purdy and Gis-
chler 2005) than an opening caused by tectonic tilting. From
1957–1958 and in 1962, atmospheric nuclear tests (H-Bombs)
were conducted directly above or near Kiritimati by the British
military and by the U.S. Army, respectively.

Recent studies focussed on carbonate-organic sediments in
brackish water lakes as related to El Niño (Trichet et al. 2001),
hydrochemistry (Saenger et al. 2006), the effect of salinity on
the D/H ratios of lipid biomarkers (Sachse and Sachs 2008),
and carbon fixation and lipid biomarkers in the microbial mats
(Büring et al. 2009). The present study concentrates on four
hypersaline lakes in the northern part of the atoll: Lake 2, 21,
22, and 51 (Figure 1). In addition, hydrochemistry data have
been obtained from further, brackish lakes, lagoonal waters,
rainwater, groundwater and seawater, with locations provided
in Figure 1.

MATERIAL AND METHODS

Hydrochemistry

Water samples for titration of total alkalinity were collected
in Schott glass bottles, and for determination of main anions and
cations in pre-cleaned PE-bottles. Samples for cation analysis
were filtered in the field through 0.8 μm membrane filters (Mil-
lipore) and fixed by acidification. Samples were stored cool
and dark until laboratory measurements. Temperature, elec-
trical conductivity, pH, and redox potential of water samples
were recorded *in situ* using a portable pH meter (WTW GmbH)
equipped with a Schott pH-electrode calibrated against stan-
dard buffers (pH 7.010 and 10.010; HANNA instruments), and
a portable conductivity meter (WTW GmbH). Dissolved oxy-
gen was analyzed titrimetrically following the Winkler method.
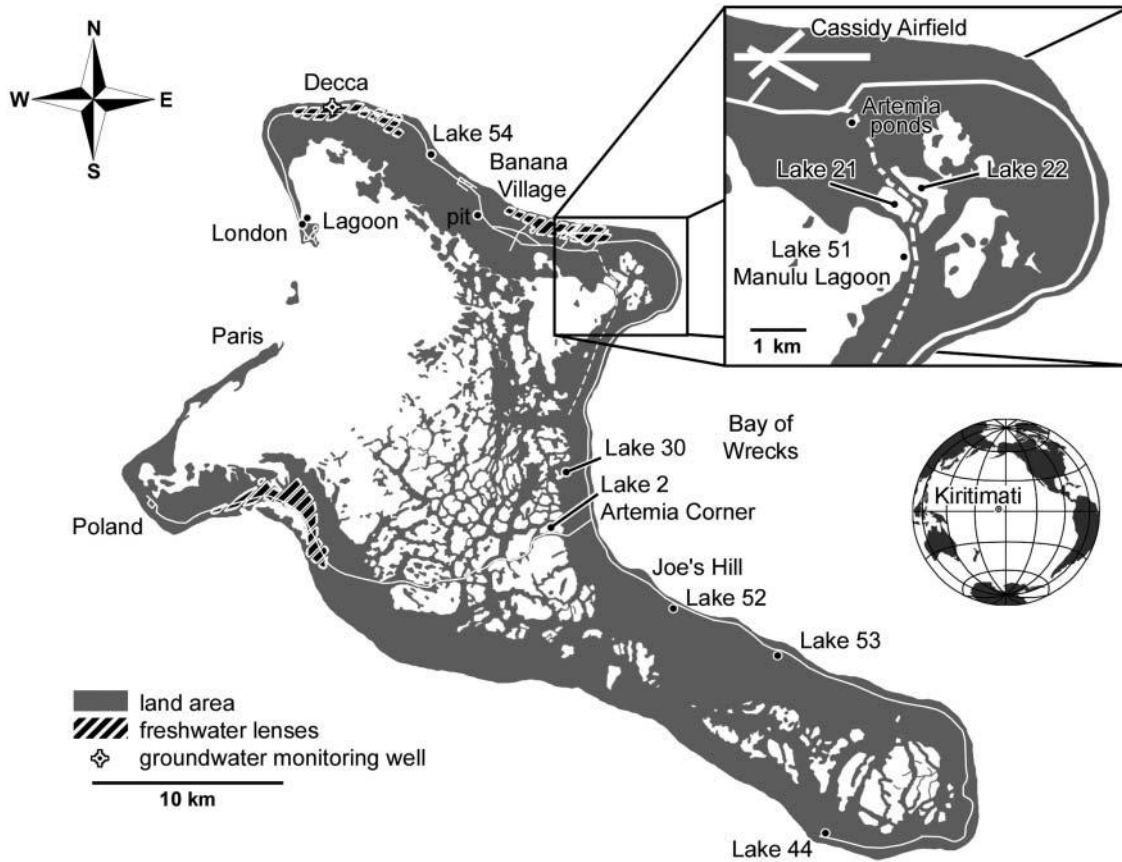
FIG. 1.   Map of the atoll of Kiritimati showing the locations investigated in this study.

Total alkalinity was determined by acid-base titration immediately after sampling using a hand-held titrator and 1.6 N H_2SO_4 cartridges as titrant (Hach Corporation).

Main cations (Ca^{2+}, Mg^{2+}, Na^+, and K^+) and anions (Cl^-, SO_4^{2-}, and NO_3^-) were analyzed by ion chromatography with suppressed conductivity detection (Dionex Corporation). ICP-OES (Perkin Elmer) was used to determine Sr^{2+} and Ba^{2+}. Dissolved phosphate and dissolved silica concentrations were measured by spectrophotometric methods (Unicam). Measured values were processed with the computer program PHREEQC
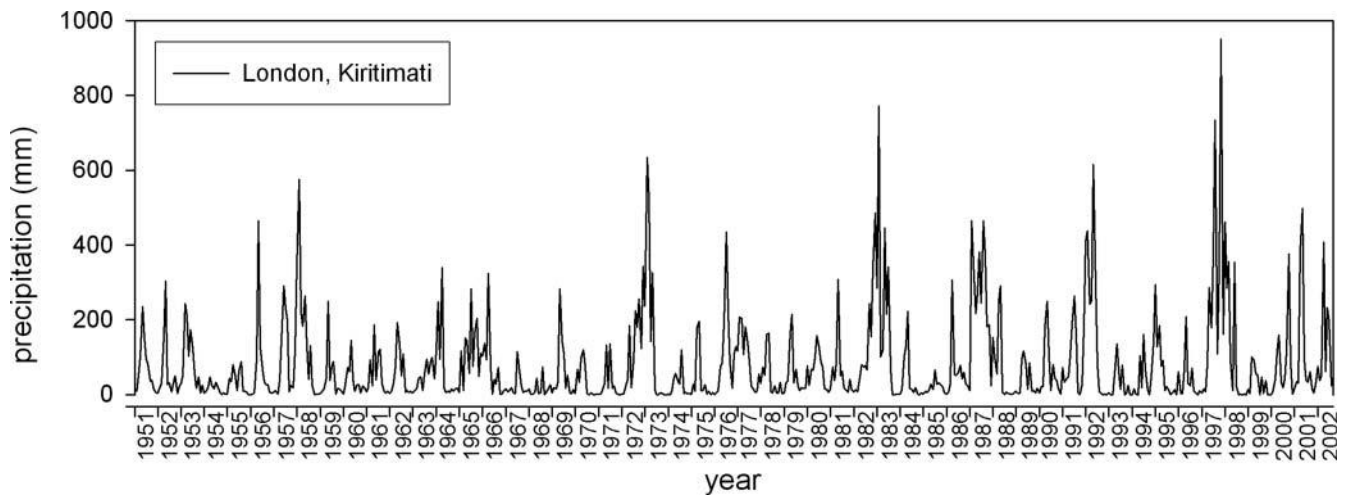
FIG. 2.   Kiritimati rainfall data for the years 1951–2002 showing El Niño Southern Oscillation (ENSO).

(Parkhurst & Appelo 1999) in order to calculate ion activities and PCO_2 of the water samples as well as saturation state with respect to calcite, aragonite and gypsum. Hydrochemical model calculations have been carried out using the same program.

Microbial Mat Fixation, Staining, Embedding and Sectioning

Microbial mat samples were collected using pre-cleaned sterile plastic cores and tubes. The samples were fixed with PBS (phosphate-buffered saline) buffered 3.7% formaldehyde for 4–8 h, rinsed with filter-sterilized PBS-buffered sampling site water, and kept cool in the dark until. After five days of transport to the home lab, samples were either stored at $4°C$ (for thin sectioning), or transferred via a graded ethanol series to 70% EtOH and frozen at $-20°C$ (for 16S rDNA analysis) until further processing. For labelling microbial cells, bulk samples were stained prior to embedding for 24 h in a 90% EtOH solution containing 3 μg/ml DAPI.

After final dehydration in a graded ethanol series, samples were embedded with LR White (LR White resin, medium grade; London Resin Company Ltd., Reading, UK) according to the manufacturer's instructions, cut with a saw microtome (Leica) to thickness of 70 μm, mounted on glass slides with Körapox (Kömmerling Chemische Fabrik GmbH, Pirmasens), and sealed by Biomount (Electron Microscopy Sciences, Hatfield, PA) and coverslips.

Phylogenetic Analysis of Prokaryotes

Phylogenetic analyzes of the prokaryotic communities were carried out using mat core samples, cut and subdivided in macroscopically different layers under a clean bench in the lab. DNA was extracted from 30–60 mm^3 aseptically cut material of each layer using the Qiagen DNeasy® Tissue Kit, following the manufacturer's protocol and eluted with 100 μl TE buffer. The PCR amplifications of 16S rRNA genes from the total DNA were performed with specific forward primers annealing at the 616 V binding site combined with universal 1525 R primer (Table 1) using the "SilverStar" Taq-polymerase (Eurogentec) or "Taq DNA polymerase" (Invitrogen). PCR assays that did not yield a clear amplicon were reamplified (nested PCR-approach) using the same forward primer and the universal 1492 R primer.

Cycling conditions in the PTC-200 (MG-Research) and Primus 96 (MWG-Biotech) cyclers were as follows: initial denaturation (2 min at $95°C$), followed by 33 cycles of denaturation (40 s at $94°C$), primer annealing (30 s + 1 s at $51°C$), elongation (2 min + 2 s at $72°C$) and a final 6 cycles of denaturation (40 s at $94°C$) and elongation (2 min at $72°C$). The PCR products purified with the EasyPure DNA Purification Kit (Biozym) were cloned into plasmid cloning vector pCR®4-TOPO®, according to the manufacturer's directions, using TOPO® TA Cloning Kit for Sequencing (Invitrogen, San Diego, California).

Competent *Escherichia coli* cells, strain DH5a were used and grown on LB medium containing ampicillin. The transformant clones were selected using α-complementation and used for PCR colony screening with M13 vector specific primers. Analytical digestions with restriction enzyme Rsa I (four cutter) were performed for the characterization of different genotypes of the clones. Inserts representing different genotypes were reamplified using M13 R and T7 F primers and subsequently purified using EasyPure DNA Purification Kit (Biozym). Both strands of DNA were sequenced using the Big Dye Terminator V2.0 Cycle Sequencing Kit with a set of sequencing primers (610RII, 609VII, 699R, T3R, T7V). Further primers used were 1492* R, 1525* R, M13 R, M13 F, and 614V. All sequencing primers are listed in Table 1.

Reactions were made in 0.2 ml plastic tubes with reaction volumes 10 μl using the PTC-200 (MG-Research) cycler. Sequencing products were run on an ABI 3100 automated sequencer according to the manufacturer's directions. The partial sequences, edited with Chromas, were subsequently assembled with the AlignIR Version 1.2 software (LI-COR). Sequencing the primary amplicon directly without cloning retrieved 11 unambiguous 16S-variants. These amplicons were obtained with universal primers and are considered to represent dominant microorganisms of the respective subsample. Using more selective primers in combination with a nested PCR approach resulted in more heterogeneous amplicons that could not be sequenced directly and had to be cloned to obtain homogeneous template DNA suitable for sequencing. Sequence data obtained directly from homogeneous PCR products were denoted with a number code preceded by "PCR", sequences retrieved via cloning were denoted with numbers preceded by "clone". Sequences were checked for possible chimeric origins by CHECK_CHIMERA software of the Ribosomal Database Project (Cole et al. 2003) and the Bellerophon Server (Huber et al. 2004; http://foo.maths.uq.edu.au/~huber/bellerophon.pl).

Sequence data were submitted to GenBank under accession numbers HM480169 to HM480268, and HQ191223. Complete 16S-sequences were compared with the GenBank nucleotide data library using megablast searches (Altschul et al. 1997; http://www.ncbi.nlm.nih.gov/blast/blast.cgi) to find the most similar sequences publicly available. For each 16S sequence the most similar GenBank entries were downloaded and incorporated into the alignment. Alignment of the sequence data was performed manually using the MEGA version 4 (Tamura et al. 2007; http://www.megasoftware.net/). Distance and phylogenetic analyzes were conducted using the same program. For phylogenetic reconstruction, the neighbor-joining method was employed and the reliability of the phylograms was assessed using bootstrap analyzes (one thousand bootstrap replicates). Bootstrap values above 70% were considered significant support for particular branches.

Microscopy

Laser-scanning microscopy of hardpart biofilm sections was carried out using a Zeiss LSM 510 Meta NLO attached to a Zeiss Axiovert 200 M, equipped with an Ar-laser, two HeNe-laser (Carl Zeiss MicroImaging, Jena), and a femtosecond-pulsed

TABLE 1

Primers used in this study for amplifying and sequencing prokaryotic 16S rDNA. F at the end of a primer name indicates the forward (5′→3′) direction, and R the reverse (3′→5′) direction

Primer name	Primer sequence 5′→3′	Specific for prokaryotic phyla	Tm (°C)	Reference
Bac-1 F	AGT TTG ATC CTG GCT CAG GAC	Actinobacteria, Chloroflexi, Bacteroidetes-Chlorobi group, Dictyoglomi, Deferribacteres, Fibrobacteres-Acidobacteria group, Firmicutes, Gemmatimonadetes	59.8	this study
Bac-2 F	AGT TTG ATC CTG GCT CAG CGC	Aquificae	61.8	this study
Bac-3 F	AG AGT TTG ATC CTG GCT CAG GAT	Bacteroidetes-Chlorobi group, Fusobacteria, Cyanobacteria	60.6	this study
Bac-4 F	AG AGT TTG ATC CTG GCT CAG AAC	Dictyoglomi, Deferribacteres, Fibrobacteres-Acidobacteria group, Nitrospirae, Planctomycetes, Spirochaetes	60.6	this study
Bac-5 F	AGT TTG ATC CTG GCT CAG GGT	Deinococcus-Thermus , Thermotogae	59.8	this study
Bac-6 F	AG AGT TTG ATC CTG GCT CAG AGT	Proteobacteria, Chlamydiae-Verrucomicrobia group	60.6	this study
Bac-7 F	AG AGT TTG ATC CTG GCT CAG ATT	Proteobacteria, Chlamydiae-Verrucomicrobia group	58.9	this study
Bac-8 F	AG AGT TTG ATC CTG GCT CAG AAT	Planctomycetes	58.9	this study
Bac-9 F	AGT TTG ATC CTG GCT CAG GGG	Thermomicrobia	61.8	this study
Bac-10 F	AGT TTG ATC CTG GCT CAG GGC	Thermodesulfobacteria	61.8	this study
CrenArchF	GG TTG ATC CTG CCG GAC C	Crenarchaeota, Korarchaeota	60.5	this study
EuArch F	GG TTG ATC CTG CCG GAG G	Euryarchaeota, Korarchaeota	60.5	this study
1492* R	CT ACG GCT ACC TTG TTA CGA C	universal	59.8	Lane 1991, modified
1525* R	GC AGG AGG TGA TCC AGC C	universal	60.5	Lane 1991, modified
M13 R	CA CAG GAA ACA GCT ATG ACC	plasmid	57.3	Sambrook & Russell 2001
M13 F	GA TGT AAA ACG ACG GCC AG	plasmid	56.7	Sambrook & Russell 2001
T3* R	CG CCA AGC TCA GAA TTA AC	plasmid	54.5	Sambrook & Russell 2001, modified
T7 V	TG AAT ACG ACT CAC TAT AGG	plasmid	53.2	Sambrook & Russell 2001
610RII	ACCGC KRCTG CTGGC AC	universal		Dotzauer et al. 2002
609VII	ACTAC YVGGG TATCT AAKCC	universal		W. Ludwig
699 R	AGGGT TGCGC TCGTT GC	Universal		W. Ludwig; Pascual et al. 2010

*Asterix indicates that primer was modified for this study.

Titan-Saphir-Laser Chameleon XR (Coherent, Dieburg). Emission fingerprinting and linear unmixing was carried out using a 32-channel diode array (Metadetector) and software of Carl Zeiss MicroImaging, Jena.

Mineralogical Analysis

The mineralogical composition of 15 microbialite and 4 mat samples was determined by X-ray diffraction analysis of whole-rock powder using a Philips instrument (control unit PW 3040, goniometer PW 3050, X-ray tube PW 3373/00, sample stage PW 1774, monochromator PW 3123/00, detector PW 3011) operating at 40 kV and 30 mA with monochromated Cu K alpha radiation (2 sec/0.02° step).

Elemental Analysis

The elemental composition of 3 microbialite samples was determined by electron microprobe analysis. Carbon-coated polished thin sections of LR-White-embedded samples were used. The analyzes were performed at 15 kV and 12 nA on a JEOL JXA 8900 RL electron microprobe at the Institute of Geochemistry, Göttingen. Ca, Mg, Sr, S, Fe and Mn were analyzed for 30 s, whereas Si, Na, and Al were analyzed for 15 s. Typical detection limits (1 σ count stat.) are 180 ppm for Na, 220 ppm for Ca, 90 ppm for Mg, 140 ppm for Sr, 150 ppm for Fe, 180 ppm for Mn, 140 ppm for S, 240 ppm for Si, and 140 ppm for Al.

Stable Isotope Analysis

Samples for carbon and oxygen stable isotope measurements have been obtained under a binocular from cutting planes (slab counterpart of thin sections) and hand specimen using a steel needle. Carbonate powders were reacted with 100% phosphoric acid (density >1.95) at 70°C using a Thermo Kiel VI carbonate preparation line connected to a Finnigan Delta plus masspectrometer. All values are reported in per mil relative to V-PDB by assigning a $\delta^{13}C$ value of $+1.95$‰ and a $\delta^{18}O$ value of -2.20‰ to NBS 19. Reproducibility was checked by replicate analysis of laboratory standards and is better than ± 0.05 (1σ). The stable isotope measurements have been carried out at the laboratory of Andreas Pack, University of Göttingen.

RESULTS

Hydrochemistry of Lake Waters and Groundwaters

Selected lakes as well as marine and meteoric waters at Kiritimati have been analyzed with respect to physical and physicochemical parameters, cations, anions and nutrients. Based on that, PCO_2 and saturation with respect to $CaCO_3$ minerals and gypsum have been calculated (Table 2). Four types of waters can be distinguished: (1) seawater and lagoonal waters, (2) brackish lakes, (3) meso- and hypersaline lakes and their pore waters, and (4) fresh to brackish groundwaters. Ternary plots of major cations and anions (Figure 3) demonstrate that all waters, except for the meteoric freshwaters, belong to Na-Cl-type, characterized by major ion ratios similar to that of seawater. For Lake 22,

salinity data are available that document a decrease in salinity from 149‰ in 1988 to 140‰ in 1990 (Trichet et al. 2001), and finally 132‰ in 2002 (this article), which probably reflect increasing El Nino intensity (Figure 2). This trend, superimposed by intermediate dry years with increased evaporation, has also been reported by Saenger et al. (2006).

The general relation of lake waters on Kiritimati in comparison to seawater is depicted by a cross-plot of Mg^{2+} versus conservative ion Na^+ (Figure 4A). This cross-plot demonstrates strict covariation of both ions, explained by evaporation of seawater, and dilution of seawater by rain water, respectively: Lagoonal seawater is slightly concentrated by evaporation from normal seawater, with highest concentrations during low tide due to reflux from distal lagoonal parts. Brackish lake waters represent seawater diluted by meteoric waters. Hypo- and hypersaline lake waters result from evaporation from seawater, and fresh to brackish groundwaters represent a mixture of meteoric freshwater and seawater (Figure 4A).

The impact of aragonite and gypsum precipitation, going along with evaporation, on seawater-derived lake waters is shown by cross-plots of Mg^{2+} versus Na^+, and Ca^{2+} versus Na^+, respectively (Figures 4A, B). The angled arrow indicates the calculated pathway of seawater evaporation plus aragonite and gypsum precipitation. With regard to hypersaline lakes, only Lake 51 (Manulu Lagoon) closely matches this model pathway, whereas Lakes 2, 21, 22 and their pore waters show higher Ca^{2+} and higher SO_4^{2-} than predicted (Figures 4B, C). The same applies to Lake 30, a mesosaline lake with microbial mats containing patchy aragonite and Mg-calcite precipitates. Hence, an increased level of inhibition of precipitation or an additional source of Ca^{2+} and SO_4^{2-} is likely for the microbialite-forming hypersaline lakes, e.g., by surface or groundwater influx.

Yet, water from a crab burrow in an artificial trench at Lake 21 (Figure 6) shows only a minor increase in Ca^{2+} concentration, but no increase in SO_4^{2-} (Figures 4B, C). In turn, some brackish lakes (pit Banana Village, Lake 53) show a relative depletion in Ca^{2+}, but not in SO_4^{2-} (Figure 4B). This coincides with high alkalinities (Figure 4D) and undersaturation with respect to gypsum (Table 2). Consequently, these values likely reflect $CaCO_3$ precipitation, ammonification and sulfate reduction in nutrient-rich groundwaters in contact with these lakes (Figure 4D).

On the contrary, the clear relation between evaporation, precipitation and Ca^{2+} concentrations, there is no correlation between Na^+ concentrations and aragonite supersaturation except for seawater and lagoonal waters (Figure 5A). However, a weak negative correlation of pH and salinities (Saenger et al. 2006) as well as a weak positive correlation is evident for pH and aragonite supersaturation (Figure 5B), with increasing pH reflecting decreasing PCO_2 (Table 2). Nonetheless, deviations from this trend are obvious: Hypersaline lakes which contain microbialites show, at similar pH, higher aragonite supersaturation values than brackish water lakes. Again this may point to a possible influx of Ca^{2+} from

TABLE 2

Hydrochemical data of seawater, lake, rain and ground waters of Kiritimati atoll. Saturation index $SI_{Calcite} = \log \Omega_{Calcite} = \log$ (ion activity product $\{Ca^{2+}\} \times \{CO_3^{2-}\}$/solubility product $K_{calcite}$)

Sample	Date	T [°C]	EC 25°C [mS cm⁻¹]	pε	pH	Alk [meq L⁻¹]	Mg/Ca [mol/mol]	Ca²⁺	Mg²⁺	Na⁺	K⁺	Sr²⁺ [mmol L⁻¹]	Cl⁻	SO₄²⁻	Si	Fe	NH₄⁺	PO₄³⁻ [μmol L⁻¹]	PCO₂ [μatm]	SI_Calcite	SI_Arag	SI_Gyp [log IAP/KT]
Seawater																						
Seawater NW' Artemia Corner	28.08.2002	29.4	52.8	5.94	8.19	2.39	5.34	10.34	55.2	472	10.2	0.0852	552	28.39	2.51	1.66	1.94	0.66	447	0.75	0.61	-0.67
Lagoon at London: high tide	05.09.2002	32.9	53.5	4.32	8.27	2.27	5.28	10.74	56.7	491	10.5	0.0871	564	28.91	2.09	0.70	0.01	0.32	331	0.82	0.68	-0.67
Lagoon at London: low tide	28.08.2002	33.0	55.8	n.d.	8.38	2.18	5.37	10.91	58.6	502	10.7	0.0898	576	30.92	2.00	1.08	1.71	0.25	219	0.86	0.72	-0.64
Brackish lakes and ponds																						
Pit NW' Banana Village: rim	28.08.2002	28.2	10.9	-0.62	9.14	14.20	24.36	0.66	16.0	110	2.1	0.0168	125	9.87	21.81	3.06	161.87	3.76	251	1.25	1.11	-1.89
Pit NW' Banana Village: centre	28.08.2002	27.9	13.8	-0.12	9.64	n.d.		n.d.	n.d.	n.d.	n.d.	n.d.	n.d.	n.d.	n.d.	n.d.	n.d.	n.d.				
Lake 53: surface	01.09.2002	36.5	24.0	4.07	8.83	7.14	25.92	1.14	29.6	202	4.5	0.0093	218	15.97	9.05	1.14	3.60	2.45	269	0.94	0.80	-1.63
Lake 54: surface	05.09.2002	31.5	24.9	4.49	8.74	2.51	7.11	3.35	23.8	182	3.8	0.0285	207	11.46	2.66	0.97	18.95	0.95	126	0.91	0.77	-1.23
Lake 52: surface	01.09.2002	37.5	32.6	5.00	8.61	3.05	3.45	9.59	33.1	281	6.4	0.0977	324	21.13	8.83	0.83	2.03	3.32	191	1.26	1.13	-0.69
Lake 44: surface	01.09.2002	37.1	32.8	4.10	8.98	2.23	4.31	7.79	33.6	282	6.2	0.0753	317	21.01	5.84	1.33	1.99	1.42	35	1.18	1.04	-0.78
Trench at Lake 21: crab burrow	04.09.2002	33.6	43.4	4.26	8.80	2.90	4.50	10.15	45.6	385	8.2	0.0823	443	24.39	6.02	1.15	55.19	3.03	83	1.26	1.13	-0.70
Artemia ponds SE' Airport	28.08.2002	31.7	49.7	4.27	8.95	3.12	7.77	7.18	55.7	440	9.9	0.0751	504	35.16	7.02	2.07	2.69	0.51	47	1.13	0.99	-0.73
Mesosaline lakes																						
Lake 30: surface	28.08.2002	36.0	61.8	0.54	8.10	3.57	4.38	17.97	78.7	638	13.9	0.1960	707	49.90	23.57	2.88	3.94	0.46	759	1.05	0.91	-0.33

(Continued on next page)

35

TABLE 2

Hydrochemical data of seawater, lake, rain and ground waters of Kiritimati atoll. Saturation index $SI_{Calcite} = \log \Omega_{Calcite} = \log$ (ion activity product $\{Ca^{2+}\} \times \{CO_3^{2-}\}$/solubility product $K_{calcite}$) (Continued)

| Sample	Date	T [°C]	EC 25°C [mS cm⁻¹]	pε	pH	Alk [meq L⁻¹]	Mg/Ca [mol/mol]	Ca²⁺	Mg²⁺	Na⁺	K⁺	Sr²⁺ [mmol L⁻¹]	Cl⁻	SO₄²⁻	Si	Fe	NH₄⁺	PO₄³⁻ [μmol L⁻¹]	PCO₂ [μatm]	SI_Calcite	SI_Arag [log IAP/KT]	SI_Gyp
Hypersaline lakes																						
Lake 2: surface	07.09.2002	32.0	124.4	4.89	7.95	3.64	4.21	38.60	162.5	1387	29.2	0.2643	1561	97.19	40.3	2.80	3.00	0.21	813	1.14	1.00	0.11
Lake 21: surface	04.09.2002	32.5	140.1	4.34	8.37	4.24	5.20	37.97	197.4	1643	34.7	0.3124	1841	113.55	31.1	1.97	2.25	0.46	224	1.44	1.30	0.13
Lake 21: 1 m depth	04.09.2002	32.4	140.1	2.87	8.36	n.d.		n.d.	n.d.	n.d.	n.d.	n.d.	n.d.	n.d.	n.d.	n.d.	n.d.	n.d.				
Lake 21: microbial mat	04.09.2002	33.6	132.0	3.27	9.03	n.d.		n.d.	n.d.	n.d.	n.d.	n.d.	n.d.	n.d.	n.d.	n.d.	n.d.	n.d.				
Lake 22: surface	04.09.2002	31.5	151.8	3.86	8.34	3.63	5.76	36.30	209.0	1753	37.6	0.3086	1991	111.77	18.1	1.23	0.31	0.52	200	1.33	1.19	0.10
Lake 22: microbial mat	04.09.2002	32.0	140.0	3.03	7.96	n.d.		n.d.	n.d.	n.d.	n.d.	n.d.	n.d.	n.d.	n.d.	n.d.	n.d.	n.d.				
Lake 51 Manulu Lagoon: surf.	29.08.2002	32.0	156.3	4.60	8.12	3.68	7.54	29.58	223.1	1876	39.5	0.2970	2153	108.38	16.9	3.83	0.27	0.98	457	1.17	1.03	−0.01
Lake 21: pore water	04.09.2002	32.6	110.8	−2.52	7.16	4.25	4.90	35.75	175.1	1500	32.0	0.2987	1736	100.83	192.4	14.68	96.56	0.93	3020	0.11	−0.03	0.08
Lake 22: pore water	04.09.2002	32.0	100.0	−2.10	7.42	5.15	10.81	25.87	279.7	2334	48.0	0.3237	2637	139.17	49.3	3.74	124.77	1.80	2570	0.50	0.37	−0.01
Rain and ground waters																						
London, rain water	29.08.2002	28.3	0.2	n.d.	7.30	0.19	0.33	0.22	0.1	1	0.0	0.0013	0	0.05	4.7	0.02	3.20	6.61	617	−1.98	−2.12	−3.53
London, well at catholic church	06.09.2002	28.7	2.1	4.88	7.36	5.87	1.38	1.95	2.69	12	0.2	0.0152	13	1.03	16.8	0.29	0.44	2.27	14791	0.25	0.11	−1.81
Decca well #10: 6 m depth	02.09.2002	30.5	0.7	7.03	7.66	4.15	2.05	0.86	1.8	2	0.1	0.0099	2	0.45	14.0	0.48	2.51	3.96	5754	0.18	0.04	−2.37
Decca well #10: 12 m depth	02.09.2002	30.1	7.8	2.13	7.51	5.87	3.67	2.35	8.6	57	1.4	0.0248	61	5.75	7.8	0.63	1.46	2.43	9550	0.28	0.14	−1.33
Decca well #10: 18 m depth	02.09.2002	29.8	28.1	1.42	7.50	3.99	4.70	6.07	28.5	239	5.2	0.0558	263	15.35	8.0	1.08	3.56	2.58	5248	0.27	0.13	−0.93
Decca well #10: 27 m depth	02.09.2002	30.4	39.2	3.66	7.52	2.96	5.03	7.99	40.2	345	7.4	0.0699	390	20.80	7.4	1.31	4.84	2.34	3467	0.22	0.08	−0.81
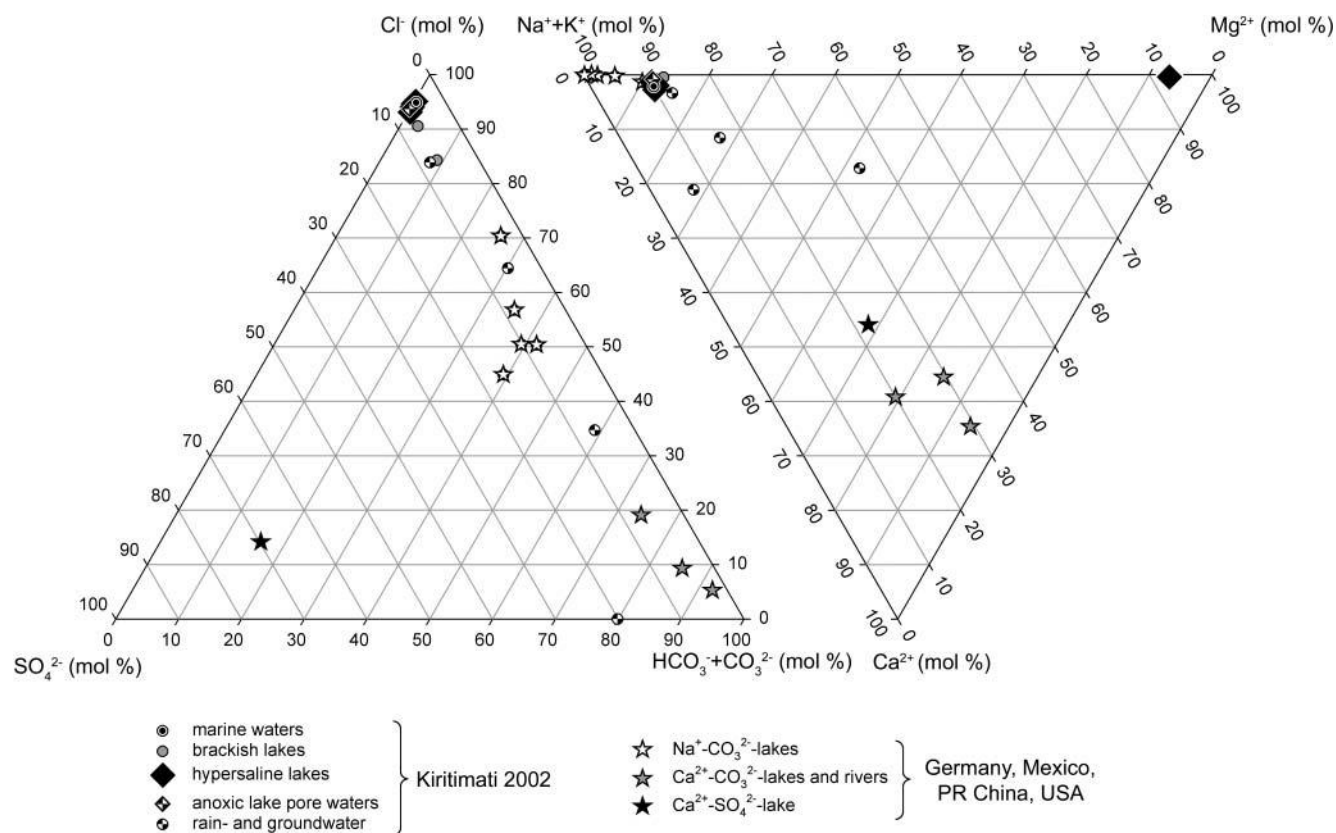
FIG. 3.   Ternary plots of mole percentages of major anions and cations from lake, pore, ground and rain waters of Kiritimati. For comparison, several microbialite-hosting lakes from Germany, Mexico, PR China and USA are shown (Winsborough et al. 1994, Arp et al. 1998, 1999, 2001), too.

subfossil carbonates via meteoric waters, and/or a high degree of inhibition of aragonite precipitation in these hypersaline lakes.

With respect to nutrients, Si, PO_4^{3-} and NH_4^+, lakes on Kiritimati show a wide range in concentrations (Table 2, Figures 5C, D). For comparison, seawater and lagoonal waters at Kiritimati are characterized by low Si, low PO_4^{3-} and NH_4^+, i.e., oligotrophic. Hypersaline lakes show very low PO_4^{3-}, low NH_4^+, but clearly increased Si relative to seawater (Figures 5C, D). Their anoxic porewaters finally show high NH_4^+ and Si concentrations, at similar PO_4^{3-}. Brackish lakes have strongly varying Si, PO_4^{3-} and NH_4^+ values (Figures 5C, D). Among them, an artificial pit near Banana Village with close contact to groundwaters shows extraordinarily high NH_4^+, possibly due to the proximity to human settlements. This may also apply to Lake 54, which is close to a cemetery.

Overview on Microbialite Occurrences

Modern calcareous microbialites investigated in this study grow in the hypersaline and hydrologically closed lakes on Kiritimati (Figures 6A, B). These are Lakes 2, 21 and 22 (Figure 1), which are cut off from seawater reflux, except for potential spillover during high sealevel. On the other hand, the hypersaline Lake 51 (Manulu Lagoon), which has a canal-like connection to

the marine lagoon, shows only fossil microbialite crusts at its dry shore. Also, all brackish to mesosaline lakes investigated in this study do not show lithified microbialites below the microbial mats, although the latter contain patchy friable $CaCO_3$ precipitates (Trichet et al. 2001).

Substrate bedrocks of the modern microbialites are, as far as visible at the shore of the different lakes, subfossil microbialite-cemented oyster beds which cover Holocene lagoonal reef debris, i.e., *Acropora* gravel with marine molluscs (Figure 7). The microbialite-cemented beds ("carbonate hardpan" in Saenger et al. 2006) show polygonal tepee structures, traceable from the dry shore to peripheral parts of the lake bottom, where their ridges of the present-day microbialites reproduce the tepees below (Figure 7). Towards the lake centre these tepee-forming Holocene carbonate crusts are apparently overlain by a gypsum bed, as encountered in digs in Lakes 21 and 22.

The thickness of microbialites varies between the lakes. In Lake 21, the microbialites are below the 3–5 cm thick microbial mat (Figures 6C, D, E) and reach thicknesses from less than 1 cm near the lake shore (3 m off the water line at 20 cm depth) to 50 cm within the lake (ca. 20 m off the water line, at 1.5 m depth; Figure 7). Intercalated are gypsum layers of 2–5 cm thickness, the most prominent approximately in the middle part of the microbialite.
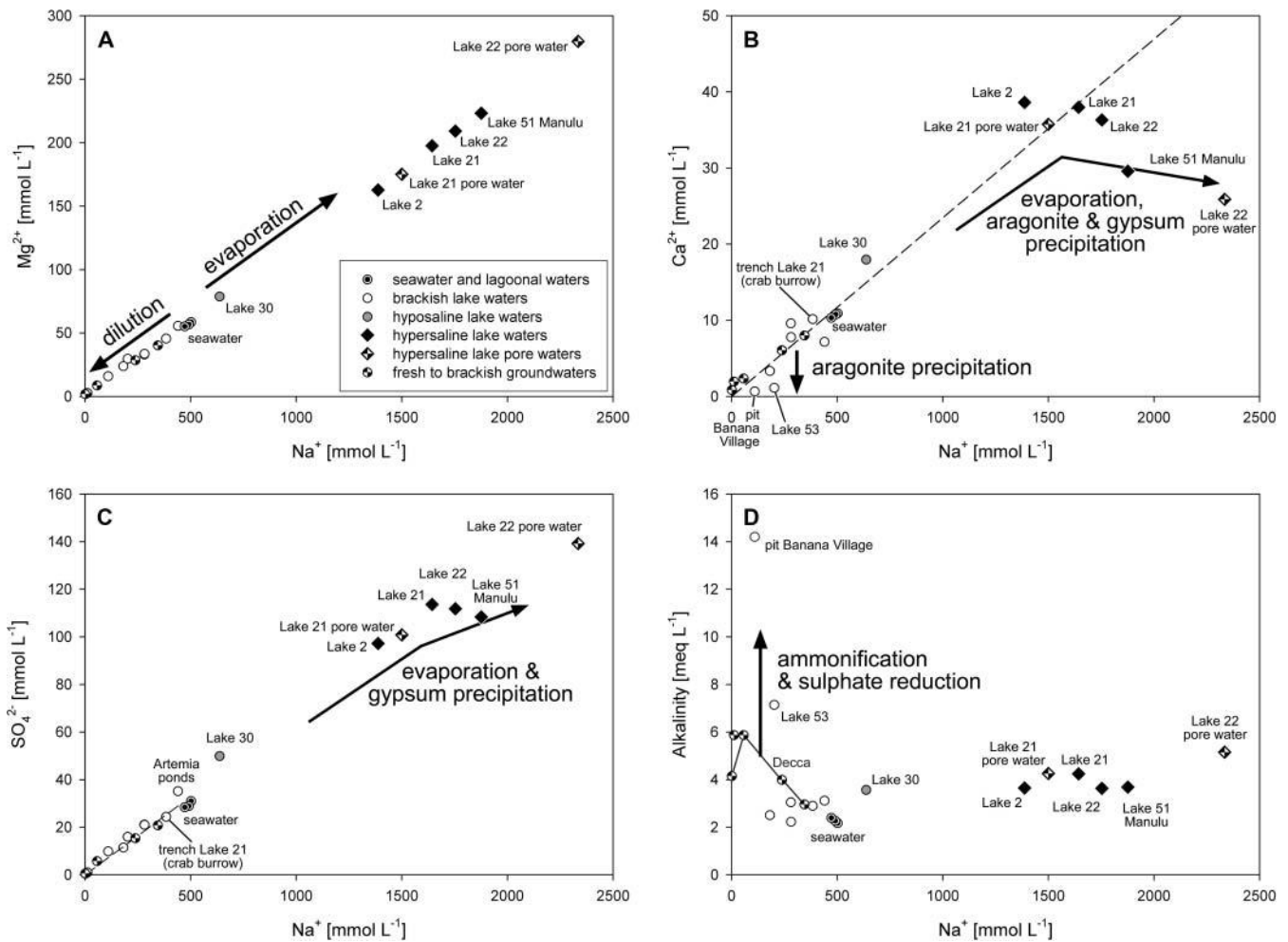
FIG. 4.   Relation of evaporation, dilution, and mineral precipitation on bulk water chemistry in Kiritimati lake, pore, and groundwaters. A. Cross-plot of Na^+ versus Mg^{2+} showing the effect of evaporation and dilution, respectively, on concentrations. B. Cross-plot of Na^+ versus Ca^{2+} showing the effect of evaporation (dashed line) and evaporation plus aragonite and gypsum precipitation (angled arrow) on Ca^{2+} concentrations. C. Cross-plot of Na^+ versus SO_4^{2-} showing the effect of evaporation (dashed line) and evaporation plus gypsum precipitation (angled arrow) on SO_4^{2-} concentrations. D. Cross-plot of Na^+ versus alkalinity showing the variable effect of ammonification and sulfate reduction on the alkalinity of the different lakes.

In Lake 22 (Figures 6A, B), calcareous microbialites are similar to that of Lake 21, but less thick and with more pronounced horizontal fabrics. The observed maximum thickness is 25 cm (ca. 20 m off the water line, at 0.5 m depth), while farther inside the lake (ca. 30 m off the water line) only 1 cm friable microbial carbonate covering a massive gypsum plate was found below the microbial mat.

In Lake 2 (Figure 6F), the microbialites are very friable and only consist of loosely cemented spherulite sands with an observed maximum thickness of 8 cm (ca. 10 m off the water line, at 0.5 m depth). No present-day microbialites have been found below the microbial mats in Lake 51 (Manulu Lagoon). Instead, platy gypsum precipitates occur at the lake bottom. Nonetheless, platelike microbialite chips are distributed

upon the tepee-structure-dissected subfossil microbialite-oyster crusts of the dry shore.

Microbial Mat Structure and Prokaryote Community

Microbial mats of hypersaline lakes attain thicknesses between 2 and 5 cm, with greatest thickness at depths more than 1 m. Here, their orange colored surfaces show tuft-like projections into the water column (Figures 6C, D). All investigated mats, i.e., mats in Lake 2, 21, 22 and 51, show an orange top layer, a green layer below, followed by a purple layer and a grey to brownish bottom zone (Figures 6E, F). With respect to molecular biological investigations, emphasis has been placed on the identity and possible function of non-phototrophic prokaryotes, while cyanobacteria were described on basis of
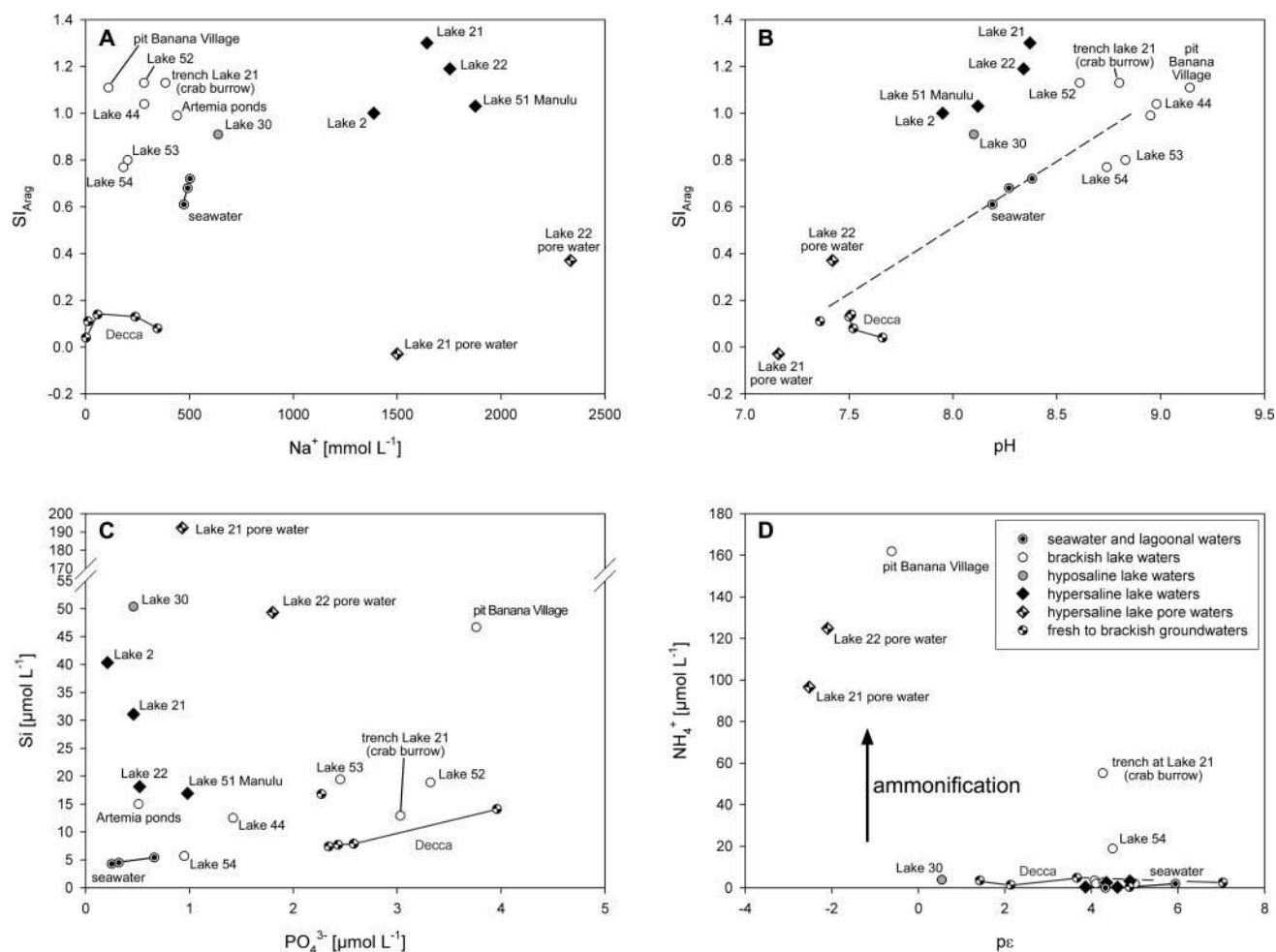
FIG. 5. Aragonite saturation index (SI_{Arag}) and nutrient conditions in Kiritimati lake, pore, and groundwaters. A. Cross-plot of Na^+ versus SI_{Arag} showing no covariation. B. Cross-plot of pH and SI_{Arag} showing a weak positive correlation of both parameters. C. Cross-plot of PO_4^{3-} versus Si demonstrating increased nutrient supply in pore waters and brackish lakes. D. Cross-plot of pε versus NH_4^+ showing increased ammonium concentrations in reducing, anoxic pore waters and water bodies in contact with anoxic groundwaters.

morphological features only. Future investigations using CARD-FISH applied to cryosections (Shiraishi et al. 2008b) are required to assign phylotypes to specific morphotypes. Based to the current data available, the distribution of prokaryotic phylotypes of the groups targeted by the primers used (i.e., exclusive *Cyanobacteria*) is shown for each layer in Figure 9.

Orange Layer

The orange layer (0–20 mm below top) is dominated by colonies of coccoid *Cyanobacteria* with more or less vertically arranged filamentous cyanobacteria in between. Cyanobacterial morphotypes comprise *Cyanothece*, *Entophysalis*, *Leptolyngbya*, *Microcoleus*, *Spirulina*, and *Johannesbaptistia*, i.e., similar to a community described from ponds of the Rangiroa atoll (Richert et al. 2006). Rarely, empty tests of diatoms of the genus *Navicula* have been encountered at the mat top. The coc-

coid morphotype *Cyanothece*, together with *Leptolyngbya*, is the dominant cyanobacterium in the orange top layer. *Cyanothece* comprises ovoid cells that are 4–5 μm in diameter and 8 μm long. Cells are commonly in pairs due to binary fission, and group in microcolonies within a poorly layered, diffuse sheath (Figure 8F). *Leptolyngbya* trichomes consist of cells 0.75–1.0 μm in diameter and 1.5–2.5 μm long, enclosed by a thin firm sheath (Figure 8B).

The total filament diameter is 1.5–2.0 μm. Empty sheath of this morphotype, probably because of their resistance against degradation, are widespread throughout the deeper mat layers. A second coccoid cyanobacterial morphotype, *Entophysalis*, is of subordinate importance in the orange top layer. *Entophysalis* is represented by colonies 20–100 μm in size, composed of spherical cells of 5–7 μm diameter. Locally, an arrangement of cells in vertical rows is evident (Figure 8B). *Microcoleus*-*Spirulina*-strands of 30–150 μm diameter are conspicuous and
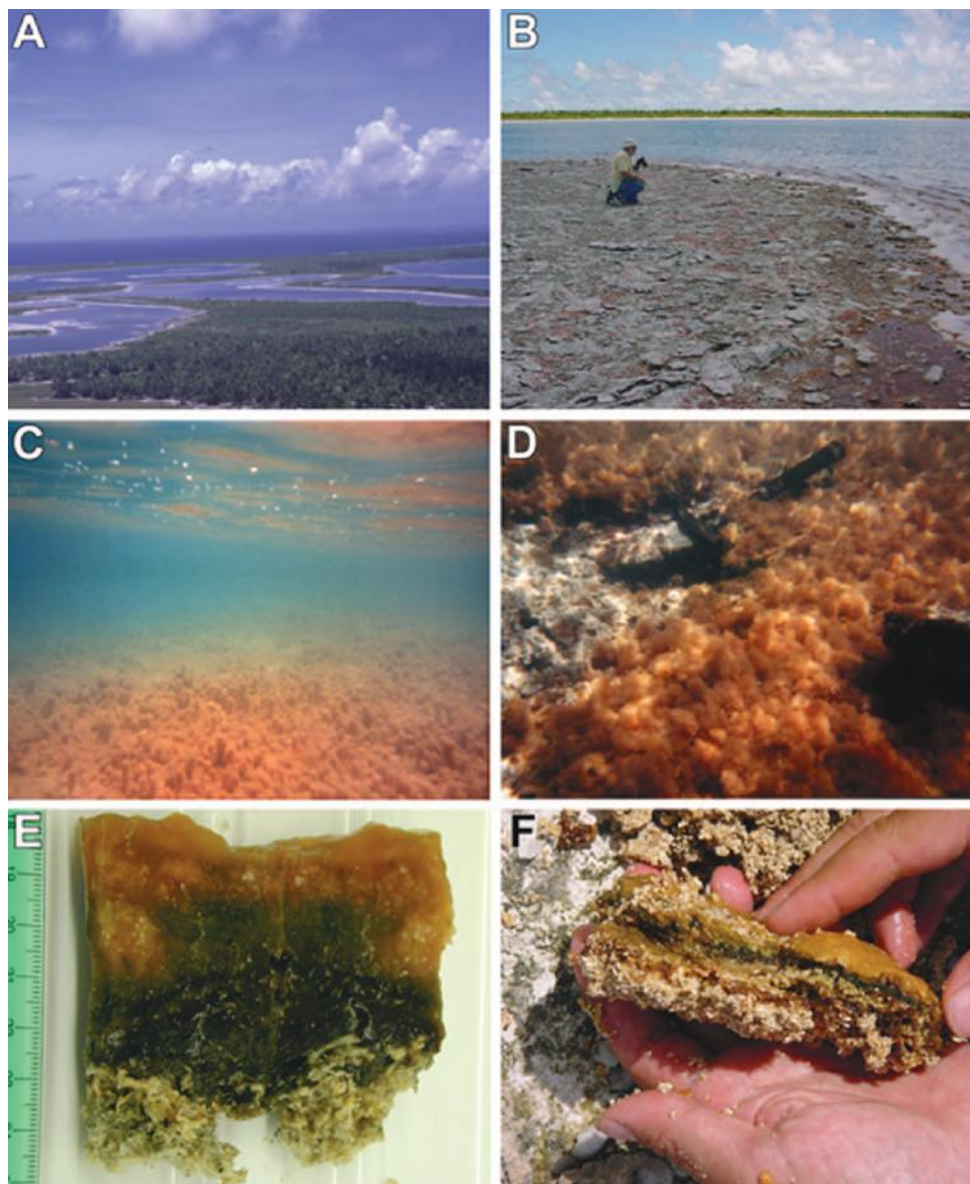
FIG. 6.   Field images of hypersaline lakes on Kiritimati and their microbial mats, August/September 2002. A. Aerial view of Lakes 21, 22, and 51 from north. B. Lake 22 dry shore showing subfossil microbial crust with tepee structures. C. Lake 21 underwater photograph showing orange colored microbial mats with tuft-like protuberance at approximately 1.5 m depth. D. Lake 21, white microbialite surface below 5-cm-thick microbial mat at approximately 40 cm depth (dig #2). E. Lake 21 dig #3 color-zoned microbial mat cut in the home laboratory, displaying spherulites in its top and middle parts, and microbialite layers in its basal part. F. Lake 2 microbial mat with clear color-zonation and white spherulitic microbialite (color figure available online).

already visible at low magnification (Figure 8C). These strands initially consist of twisted *Microcoleus* trichomes (3.5–4.0 μm in diameter, with cells 4.3–6.6 μm long, cell walls being slightly constricted), which are increasingly associated with numerous *Spirulina* trichomes (1.5 μm cell diameter), all enclosed within a common sheath envelope. Large strands finally show abundant *Spirulina* with only few *Microcoleus* trichomes. The surface of the common sheath envelope shows numerous attached non-phototrophic bacteria.

A peculiar, though less abundant morphotype in the orange layer, is *Johannesbaptistia pellucida*. Its discoid to half-spherical cells of 8–15 μm diameter are arranged in one row within a common sheath and form slightly wavy pseudofilaments (Figure 8D). Few pseudofilaments are scattered throughout the orange and green layer. Only between 13–19 mm below the top of the mat (i.e., deeper part of the orange layer) this morphotype is common. In general, the genus *Johannesbaptistia* is known to occur in tropical, heliothermal water bodies
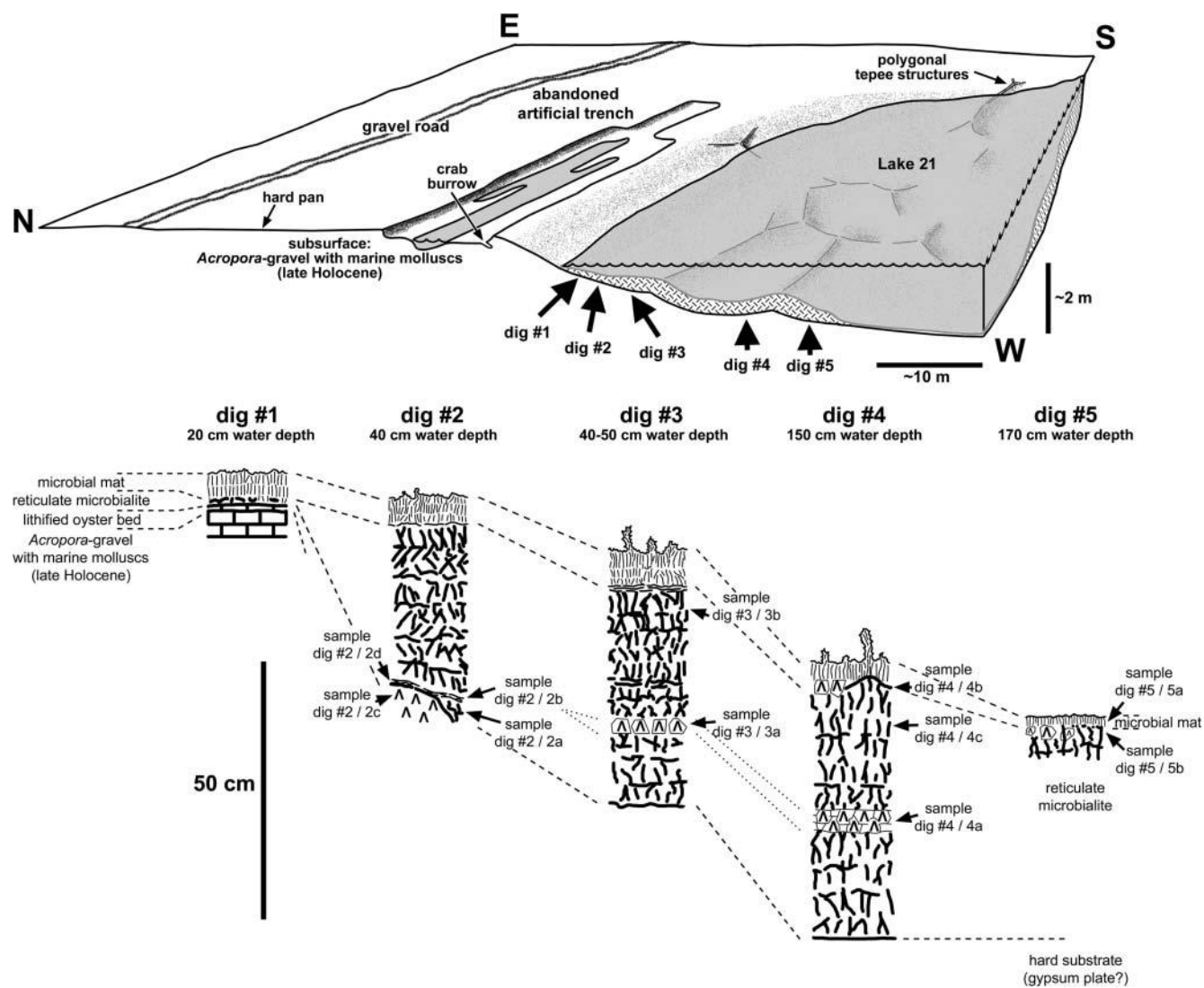
FIG. 7. Geological-hydrological setting of marginal parts of the hypersaline Lake 21 with its microbialites, August/September 2002.

poor in nutrients, and in Yellowstone thermal springs (Komárek and Anagnostidis 1999). The coccoid morphotype *Chroococcus*, in the orange top layer with only scattered occurrence, shows spherical to semispherical cells of 2.0–3.5 μm diameter.

Colonies of 10–20 μm diameter consist of 4–16 cells. Characteristic are successive binary fissions that result in packages of 4–8 cells, and a clear firm sheath enclosing the cell packages (Figure 8E). A second species with 5–10 μm cell diameter was found in top parts of Lake 22 microbial mat. Thin sheathless filaments of 0.5 μm diameter, with 1.2–2.0 μm long cells, which occur throughout this layer and the green layer below, may represent *Chloroflexi*. Between the phototrophs, numerous coccoid, rod-shaped and filamentous bacteria are distributed (Figure 8E, F).

The 16S rDNA sequences obtained from the orange layer (Table 3, Figures 9, 10) demonstrate the presence of *Alphaproteobacteria*, among them representatives of the *Rhi-*

zobiales, which comprise endophytes as well as rhizosphere bacteria (*Phyllobacterium myrsinacearum* FJ405362, *Mesorhizobium* sp. AJ2950). In addition, a close relative of *Methylobacterium populi*, i.e., a pink-pigmented aerobic, facultatively methylotrophic, methane-utilizing bacterium (Van Aken et al. 2004; Green 2006) has been detected. Furthermore, a relative of *Caulobacter* (with 97% sequence similarity to insect intestine clone D AJ459874) and one clone of the order *Sphingomonadales* were obtained. Both, *Caulobacterales* and *Sphingomonadales*, are aerobic chemoorganotrophs common in oligotrophic aquatic habitats (e.g., Staley et al. 1987; Stahl et al. 1992; Cavicchioli et al. 1999).

Betaproteobacteria are represented by several clones of the order *Burkholderiales*, which comprises genera known as soil bacteria as well as plant symbionts or pathogens to plants and animals (Palleroni 2005). *Firmicutes* are represented by relatives of the halophilic *Pontibacillus* (PCR Kir21org 11-211103
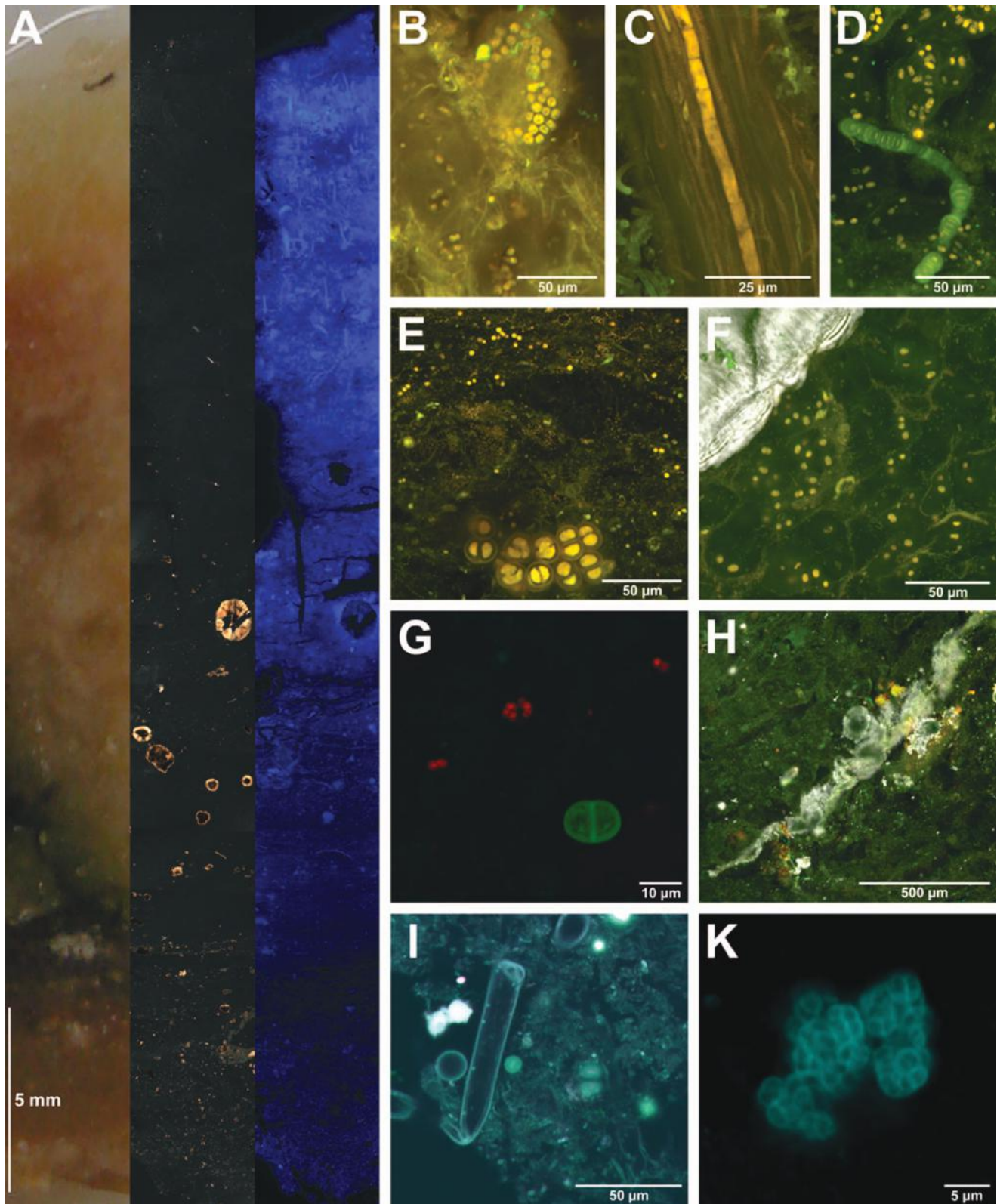
FIG. 8. Mat structure and prokaryote communities. A. Vertical section through microbial mat of Lake 21, dig 3. Left column: plain view to show color zonation. Middle column: microbial mat section in transmitted light view with crossed polarizers to show mineral components (microcrystalline aragonite, spherulites). Right column: same view under epifluorescence (excitation 365 nm, emission 397–700 nm) to show general distribution of microbial cells stained by DAPI.

with 97% sequence similarity to *Pontibacillus* sp. TB138) and the microaerophilic carbohydrate fermenting *Aerococcus* (clone Kir21org aB1.22 with 99% sequence similarity to the halotolerant *Aerococcus* sp. P3-2). In addition, close relatives (clones aB1.6 and aB3.3) of *Rhodococcus erythropolis* (99% sequence similarity), an actinobacterial taxon that can metabolize aromatic compounds (e.g., Lenke et al. 1992), were detected in the orange layer.

Green Layer

The green layer shows abundant colonies of the cyanobacterial morphotype *Cyanothece* which are largely in the state of dying and decay. Instead, *Chroococcus* colonies ("large morphotype") are common (Figure 8E), associated with few *Johannesbaptistia* pseudofilaments. 3.5- to 4-μm-sized coccoid cyanobacterial cells with individual 2-μm-thick sheaths (small *Chroococcus* morphotype) are distributed throughout the layer, while filamentous *Cyanobacteria* are rare and largely restricted to empty sheaths of *Leptolyngbya*. In general, this layer shows a successive degradation of the primary exopolymer fabric, with increasing horizontal structure and spatial enrichment of carbonate particles (Figure 8A). Numerous coccoid, rod-shaped and filamentous non-phototrophic bacteria occur throughout the layer.

The 16S rDNA sequences obtained from the green layer (Table 3, Figures 9, 10) show a dominance of alpha- and betaproteobacterial taxa with respect to the non-cyanobacterial prokaryotic community. Among the *Alphaproteobacteria*, members of the *Sphingomonadales* are now most common, while members of the *Rhizobiales* and *Caulobacterales* remain present. The *Betaproteobacteria* are, similar to the orange top layer, largely represented by members of the *Burkholderiales*, with close relatives from soils. One betaproteobacterial partial clone sequence (clone Kir21grn bB8.2*) was found to be 96% identical to the uncultured bacterium AY053477, which was associated with marine gas hydrates (Gulf of Mexico; Lanoil et al. 2001).

Two clones of *Gammaproteobacteria* have been detected, with close relatives to uncultivated bacteria from seafloor hydrothermal vent and settings of anaerobic ammonium oxidation, respectively. Also, *Bacteriodetes*, yet without evidence in the orange top layer, occur in the green layer. Their nearest relatives are known from microbial mats of hypersaline and sulfidic environments, respectively. Again, one clone with 99% sequence similarity to *Rhodococcus erythropolis* was retrieved. Conspicuous is the presence of representatives of the candidate division TM6, detected by several clones. Similar to the orange top layer, sequences obtained from PCR products using universal primers demonstrate the abundance of halophilic *Firmicutes* of the genus *Pontibacillus*. One clone (clone 21gfCA.1*) could be assigned to the phylum *Crenarchaeota* and showed 99% sequence similarity with an uncultured crenarchaeote from a hypersaline pond microbial mat of Guerrero Negro, Baja California (Robertson et al. 2009).

Purple Layer

The purple layer is characterized by abundant empty spheroidal cell envelopes of 10 μm diameter and with binary fission (Figure 8G). They likely present sheaths of dead cyanobacterial cells of the small *Chroococcus* variety mentioned from the green layer. Cell groups of the large *Chroococcus* variety are still common. Due to their autofluorescence characteristics, spherical cells of 2 μm diameter, commonly in groups of 2–8 cells, are likely purple bacteria (Figure 8G). Numerous empty cyanobacterial sheaths, predominantly *Leptolyngbya*, occur besides of abundant rod-shaped bacterial cells of 1.0–1.5 μm size.

Only few 16S rDNA sequences are available from this layer (Table 3, Figures 9, 11). Sequences obtained from PCR products using universal primers (PCR Kir51pur 18-211103; Kir21pur 7-211103) indicate the abundant occurrence of halophilic *Firmicutes* of the genus *Pontibacillus* in this layer from both lakes, 51 and 21. In addition, one clone (Kir21pur d37), with 99% sequence similarity to clone ET5_1G3 from a microbial mat of Guerrero Negro, Baja California (Orphan et al. 2008), demonstrates the presence of *Thermoplasmatales*.

FIG. 8. *(Continued)* B. Mat top with *Entophysalis*, *Cyanothece* and thin filamentous cyanobacteria (*Leptolyngbya*). Top of orange layer. LSM micrograph (excitation 488, 543, 633 nm / emission 500–530, 565–615, 640–700 nm, projection of 21 planes at 1 μm z distance). C. Consortium of *Microcoleus* (here a single trichome) and *Spirulina*, surrounded by empty *Leptolyngbya* sheaths. Middle part of orange layer. LSM micrograph (excitation 488 nm, 543 nm, 633 nm / emission 500–530, 565–615, 640–700 nm, projection of 21 planes at 1 μm z distance). D. *Johannesbaptistia* between *Cyanothece* colonies and thin filamentous photosynthetic bacteria. Deeper part of orange layer, 13mm below top of microbial mat. LSM micrograph (excitation 488, 543, 633 nm / emission 500–530, 565–615, 640–700 nm, projection of 11 planes at 1 μm z distance). E. *Chroococcus* colonies and numerous small coccoid and filamentous cyanobacteria in middle part of green layer. Note horizontal structure of exopolymer matrix. LSM micrograph (excitation 488, 543, 633 nm / emission 500–530, 565–615, 640–700 nm, projection of 15 planes at 1 μm z distance). F. *Cyanothece* colonies associated with filamentous and rod-shaped non-phototrophic bacteria. Upper left corner shows margin of large aragonite spherulite. Deeper part of orange layer, 16 mm below top of microbial mat. LSM micrograph, overlay of epifluorescence (excitation 488, 543, 633 nm / emission 500–530, 565–615, 640–700 nm, projection of 11 planes at 0.5 μm z distance) and X Nicols. G. Purple bacteria and dead empty cells of coccoid cyanobacteria of the purple layer. LSM micrograph (excitation 488 nm, emission 490–700 nm, spectral detection) after linear unmixing. Emission maximum 550 nm shown in green, 590 nm shown in red. H. Oblique band of aragonite precipitates between purple bacteria, cyanobacteria and non-phototrophs. Purple layer, 28 mm below top of microbial mat. LSM micrograph, overlay of epifluorescence (excitation 488, 543, 633 nm / emission 500–530, 565–615, 640–700 nm) and X Nicols. I. Overview of the basal anaerobic mat part with empty cyanobacterial sheaths, numerous bacterial cells and tube-shaped insect remains. Grey-brownish basal layer of microbial mat. 2P-LSM micrograph (excitation 720 nm / emission 435–485 nm). DAPI stained. K. Sarcina-like prokaryote colony from brownish basal layer of microbial mat. 2P-LSM micrograph (excitation 720 nm / emission 435–485 nm). DAPI stained (color figure available online).
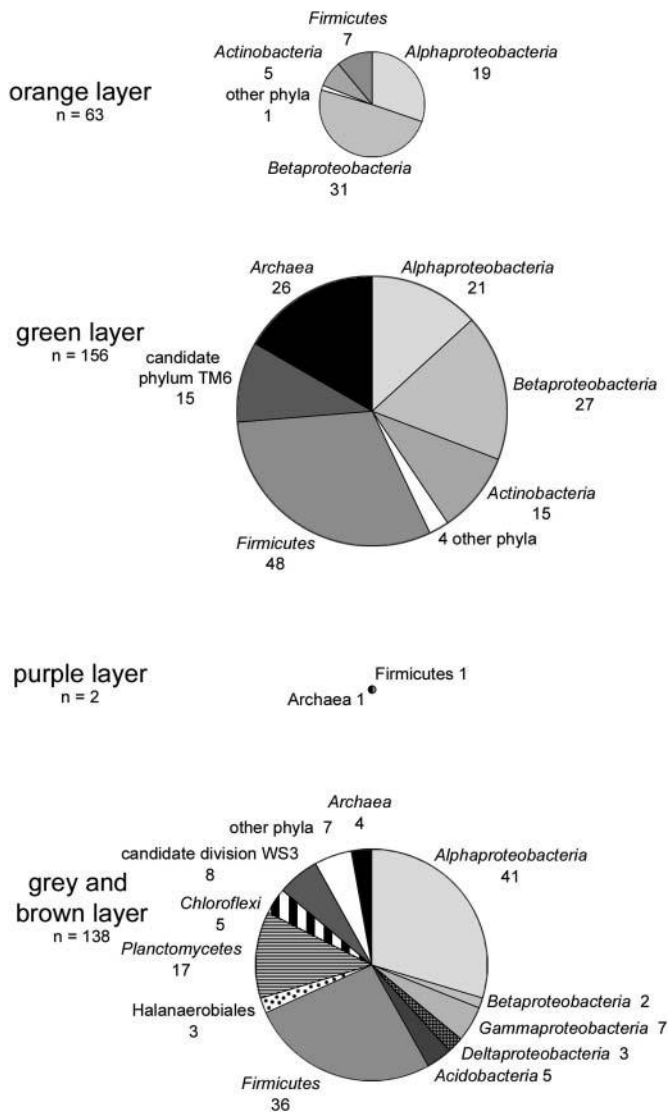
FIG. 9.   Distribution of prokayotic phylotypes exclusive *Cyanobacteria* (full and partial 16S rDNA sequences) within orange, green, purple, grey and brown layers from the microbial mat of Lake 21.

Grey and Brown Layers

The grey bottom zone of the mats and brownish floccu-lent EPS of microbialite pore spaces exhibit numerous coc-coid and rod-shaped non-phototrophic bacterial cells 1–2 μm in size. Occasionally, sarcina-like cell aggregates were observed (Figure 8K).

For the grey layer, most sequences were obtained for the *Alphaproteobacteria* and *Firmicutes* (Table 3, Figures 9, 11). Among the *Alphaproteobacteria*, one clone could be assigned to the *Rhodobacterales*, a group which comprises the non-sulphur purple bacteria. Most alphaproteobacterial clones of this layer, however, are members of the *Rhizobiales*, with close relatives described from a hypersaline microbial mat of Puerto Rico (Isen-

barger et al. 2008). One clone showed 99% sequence similarity to *Methylobacterium fujisawaense* DSM5686 AY169421.1.

This species grows on methanol and thiosulfate in nutrient-limited mixotrophic conditions (Anandham et al. 2009). *Be-taproteobacteria* are represented by a relative of *Janthinobac-terium lividum*, known from soil and water samples. This taxon is known to produce chitinases (Gleave et al. 1995) (note insect remain in this mat part shown in Figure 8I).

In addition, single clones of the *Gammaproteobacteria*, *Aci-dobacteria* and *Chloroflexi* (green non-sulfur bacteria) were de-tected. Several clones as well as a sequence obtained directly from PCR products indicate the abundance of *Firmicutes* of the *Pontibacillus-Halobacillus* clade. Also, *Halanaerobiales* and *Clostridiales* are present, as proven by single clones. The latter order is represented by a relative of the strictly anaerobic *Desul-fonispora thiosulfatigenes* DSM 11270 (91% sequence similar-ity), which is capable of desulfonation as well as producing actate, ammonia and thiosulfate (Denger et al. 1999). Several clones could be assigned to the candidate divisions TM6 and KSB1, with closest relatives known from other hypersaline mi-crobial mats (Isenbarger et al. 2008), sulfide-containing springs (e.g., AB425065; Horath et al., unpublished) or hydrocarbon-containing sediments (Winderl et al. 2009).

Furthermore, clones with next relatives of uncertain phyloge-netic position (Knittel et al. 2003) or provisionally arranged as "hypersaline group II (HS-II)" (Lloyd et al. 2006) were found. All of them are described from saline to hypersaline methane seepage sites. *Planctomycetes*, absent from the higher mats parts in Kiritimati lakes 21 and 51, occur in the grey layer, again with close relatives from hypersaline or methane-bearing settings, respectively. The same applies to the two *Crenachaeota* clones detected, with next relatives from Guerrero Negro hypersaline microbial mat (Robertson et al. 2009) and anaerobic mud of a Mediterranean mud volcano (FJ649533; Kormas et al., unpub-lished). Microbial methane production is finally indicated by a *Euryarchaeota* sequence obtained directly from PCR prod-uct of this layer, with 97% sequence similarity to the methy-lotrophic *Methanohalophilus mahii* from Great Salt Lake anaer-obic sediments (Paterek and Smith 1988) and 98% sequence similarity to *Methanohalophilus euhalobius* X98192 from saline subsurface waters of a Russian oil field (Davidova et al. 1997).

The 16S rDNA sequences obtained from the brown flocculent microbial aggregates at the top of Lake 21 microbialites demon-strate the presence of *Alphaproteobacteria*, among them mem-bers of the *Rhizobiales* and *Caulobacteriales* (Table 3, Figures 9, 11). Again, one clone with 99% sequence similarity to *Methy-lobacterium fujisawaense* DSM5686 was retrieved. *Betapro-teobacteria* comprise a member of the *Burkholderiales* with a distant relative from a soil. Two *Gammaproteobacteria* clones are closely affiliated with marine *Pseudomonas* stains. *Firmi-cutes* are again represented by members of the *Halobacillus-Pontibacillus* group, two of them with close relatives from Cabo Rojo hypersaline microbial mat. Also, one clone of the

TABLE 3

Operational taxonomic units (OTUs) retrieved from Kiritmati microbial mats and their nearest relatives with percentage identity to first match through BLASTn

OTU	Nearest neighbor	Accession #	Location and habitat	Sequence similarity	Systematic position
(1) orange layer					
clone Kir51org cB1.4	*Phyllobacterium myrsinacearum* SPc	FJ405362	Washington, surface sterile sweet potato plants	99%	Alphaproteobacteria, Rhizobiales
clone Kir21org aB1.2	*Phyllobacterium* sp. EBBLQ01	FJ178785	China, Fengyang Moutain nature reserve, endophyte	99%	Alphaproteobacteria, Rhizobiales
clone Kir21org aB4.10	*Mesorhizobium amorphae* SEMIA 6430	FJ025124	Brazil, root nodule of *Acacia angustissima*	99%	Alphaproteobacteria, Rhizobiales
clone Kir21org aB3.7	Cabo Rojo mat clone MAT-CR-P1-D09	EU246005	Puerto Rico, Cabo Rojo, hypersaline microbial mat	99%	Alphaproteobacteria, Rhizobiales
clone Kir21org aB10.24	*Bradyrhizobium* sp. SEMIA 6093	FJ390909	Brasilian SEMIA Culture Collection, host *Aeschynomene americana*	99%	Alphaproteobacteria, Rhizobiales
clone Kir51org cB10.2	*Methylobacterium populi* BJ001	NR.029082	Michigan, from poplar tree *Populus deltoides × nigra*	99%	Alphaproteobacteria, Rhizobiales
clone Kir21org aB10.25	insect intestine clone D	AJ459874	coleopteran larval intestine (*Zophobas mori*)	97%	Alphaproteobacteria, Caulobacterales
clone Kir51org cB4.1	South China Sea clone S-5m-101	GU061917	South China Sea, seawater	98%	Alphaproteobacteria, Sphingomonadales
clone Kir21org aB6.15	clone Om_02_O04B	EU137464	Colorado, ground squirrel flea *Oropsylla montana*	99%	Betaproteobacteria, Burkholderiales
clone Kir21org aB8.40	MOR bacterium L188S.605	EU935269	MOR, Liliput hydrothermal field, sediment	99%	Betaproteobacteria, Burkholderiales
clone Kir21org aB8.37	clone Om_02_O04B	EU137464	Colorado, ground squirrel flea *Oropsylla montana*	99%	Betaproteobacteria, Burkholderiales
clone Kir51org cB7.3	clone Om_02_O04B	EU137464	Colorado, ground squirrel flea *Oropsylla montana*	99%	Betaproteobacteria, Burkholderiales
clone Kir21org aB8.43	clone Om_02_O04B	EU137464	Colorado, ground squirrel flea *Oropsylla montana*	99%	Betaproteobacteria, Burkholderiales
clone Kir21org aB7.26	soil Betaproteobacterium PII_GH1.2.A10	AY162057	Ghana, tropical forest soil	98%	Betaproteobacteria, Burkholderiales
clone Kir51org cB7.1	*Ralstonia solanacearum* HZ-1	EF585144	China, pathogen of potato *Solanum tuberosum*	95%	Betaproteobacteria, Burkholderiales
clone Kir21org aB1.6	*Rhodococcus erythropolis* PR4	AP008957	Pacific, S of Okinawa, deep sea 1000 m depth	99%	Actinobacteria, Actinomycetales
clone Kir21org aB3.3	*Rhodococcus erythropolis* HS8	AY168586	United Kingdom, explosive contaminated land	99%	Actinobacteria, Actinomycetales
clone Kir21org aB1.22	*Aerococcus* sp. P3-2	EU376006	Grenada, on Parrotfish *Sparasoma viridae*	99%	Firmicutes, Lactobacillales
PCR Kir21org 11-211103	*Pontibacillus* sp. TB138	EU308474	Western Greece, solar saltern	97%	Firmicutes, Bacillales
(2) green layer					
clone Kir21grn eB4.5	Cabo Rojo mat clone MAT-CR-P1-D09	EU246005	Puerto Rico, Cabo Rojo, hypersaline microbial mat	95%	Alphaproteobacteria, Rhizobiales
clone Kir51grn dB10.3	insect intestine clone D	AJ459874	coleopteran larval intestine (*Zophobas mori*)	98%	Alphaproteobacteria, Caulobacterales
clone Kir51grn dB1.4	Coco's Island clone S25.314	EF573970	Costa Rica, site S25 near Coco's Island	98%	Alphaproteobacteria
clone Kir21grn bB4.3	high-CO$_2$ *Sphingomonas* sp. YT0136	AB362778	Japan, Kanagawa Prefecture, water/soil, high CO$_2$	96%	Alphaproteobacteria, Sphingomonadales
clone Kir51grn dB4.2	humic lake clone CrystalBog022E8	AY792291	Northern Wisconsin, humic freshwater lake	98%	Alphaproteobacteria, Sphingomonadales
clone Kir21grn bB4.4	Camargue mat *Sphingomonas* sp.	DQ218322	France, Camargue, estuarine microbial mats	98%	Alphaproteobacteria, Sphingomonadales
clone Kir21grn eB8.2	crab intestine clone C1E	DQ856499	China, intestinal microflora in Chinese mitten crab	99%	Alphaproteobacteria, Sphingomonadales
clone Kir21grn bB8.2*	Gulf gas hydrate clone AT425.Eub48	AY053477	Gulf of Mexico, anaerobic mud with gas hydrate	96%	Betaproteobacteria

TABLE 3

Operational taxonomic units (OTUs) retrieved from Kiritmati microbial mats and their nearest relatives with percentage identity to first match through BLASTn (*Continued*)

OTU	Nearest neighbor	Accession #	Location and habitat	Sequence similarity	Systematic position
clone Kir51grn dB7.2	fish intestine clone F1F	DQ860023	China, fish intestinal microflora	99%	Betaproteobacteria
clone Kir21grn bB6.5	soil *Burkholderia* sp. PSB10	EU184087	France, rhizospheric soil	95%	Betaproteobacteria, Burkholderiales
clone Kir21grn bB6.1	soil clone HF_C_1	FJ624874	Finland, boreal pine forest soil	99%	Betaproteobacteria, Burkholderiales
clone Kir51grn dB6.1	Lau hydrothermal vent clone DYB11	EU982450	Pacific, Lau Basin hydrothermal vent sediment	99%	Gammaproteobacteria
clone Kir21grn eB7.1	anammox reactor clone KIST-JJY048	EF659421	Koreao, suspended sludge from anammox reactor	93%	Gammaproteobacteria
clone Kir21grn eB7.3	Cabo Rojo mat clone MAT-CR-H2-H11	EU245143	Puerto Rico, Cabo Rojo, hypersaline microbial mat	92%	Bacteroidetes
clone Kir21grn eB8.1	Frasassi Cave mat clone FC1_16S_93	EU662503	Italy, Frasassi Caves, microbial mat from sulfidic cave	90%	Bacteroidetes
clone Kir21grn bB4.5*	*Rhodococcus erythropolis* PR4	AP008957	deep sea, 1000 m depth, S of Okinawa, Pacific Ocean	99%	Actinobacteria, Actinomycetales
clone Kir21grn eB6.1	Arvadi spring clone 17-90-ArvAB	AB425065	Switzerland, central Alps, Arvadi spring biofilm	90%	candidate division TM6
clone Kir21grn eB3.3*	Arvadi spring clone 17-90-ArvAB	AB425065	Switzerland, central Alps, Arvadi spring biofilm	92%	candidate division TM6
clone Kir21grn eB7.2*	Arvadi spring clone 17-90-ArvAB	AB425065	Switzerland, central Alps, Arvadi spring biofilm	92%	candidate division TM6
clone Kir21grn eB6.3*	Arvadi spring clone 17-90-ArvAB	AB425065	Switzerland, central Alps, Arvadi spring biofilm	93%	candidate division TM6
clone Kir21grn eB8.5	Arvadi spring clone 17-90-ArvAB	AB425065	Switzerland, central Alps, Arvadi spring biofilm	90%	candidate division TM6
clone Kir21grn eB8.3	Ebro Delta mat clone IE037	AY605134	Spain, Ebro Delta microbial mat	98%	Spirochaetes, Spirochaetales
clone Kir21grn eB4.2	*Pontibacillus* sp. TB138	EU308474	Western Greece, solar saltern	99%	Firmicutes, Bacillales
PCR Kir21grn 3-211103	*Pontibacillus* sp. TB138	EU308474	Western Greece, solar saltern	99%	Firmicutes, Bacillales
PCR Kir51grn 7-211103	*Pontibacillus* sp. TB138	EU308474	Western Greece, solar saltern	97%	Firmicutes, Bacillales
PCR Kir21grn 2-21103	*Pontibacillus* sp. TB138	EU308474	Western Greece, solar saltern	97%	Firmicutes, Bacillales
clone Kir21grn fCA.1*	Guerrero Negro mat clone GNA05C02	EU731965	Mexico, Guerrero Negro hypersaline microbial mat	97%	Crenarchaeota
(3) purple layer					
PCR Kir51pur 18-211103	*Pontibacillus halophilus* JSM 076056	EU583728	South China Sea, sea urchin	99%	Firmicutes, Bacillales
clone Kir21pur d37	Guerrero Negro mat clone ET5_1G3	EU585961	Mexico, Guerrero Negro hypersaline microbial mat	97%	Euryarchaeota, Thermoplasmatales
(4) grey layer					
clone Kir51gry B2.b34	Cabo Rojo mat clone MAT-CR-P6-E07	EU246298	Puerto Rico, Cabo Rojo, hypersaline microbial mat	97%	Alphaproteobacteria, Rhodobacterales
clone Kir21gry B8.b16	Guerrero Negro mat clone 072DZ18	DQ330987	Mexico, Guerrero Negro hypersaline microbial mat	99%	Alphaproteobacteria
clone Kir51gry B2.b32	Cabo Rojo mat clone MAT-CR-P1-D09	EU246005	Puerto Rico, Cabo Rojo, hypersaline microbial mat	94%	Alphaproteobacteria, Rhizobiales
clone Kir21gry B7.c14	Cabo Rojo mat clone MAT-CR-P1-D09	EU246005	Puerto Rico, Cabo Rojo, hypersaline microbial mat	99%	Alphaproteobacteria, Rhizobiales
clone Kir51gry B2.c41	Cabo Rojo mat clone MAT-CR-P1-D09	EU246005	Puerto Rico, Cabo Rojo, hypersaline microbial mat	97%	Alphaproteobacteria, Rhizobiales

46

Clone	Closest match	Accession	Source	Similarity	Taxonomy
clone Kir21gry B8.b15	Cabo Rojo mat clone MAT-CR-P1-D09	EU246005	Puerto Rico, Cabo Rojo, hypersaline microbial mat	97%	Alphaproteobacteria, Rhizobiales
clone Kir51gry B4.a19	Cabo Rojo mat clone MAT-CR-P1-D09	EU246005	Puerto Rico, Cabo Rojo, hypersaline microbial mat	96%	Alphaproteobacteria, Rhizobiales
clone Kir21gry B4.c54	Methylobacterium fujisawaense 1-44	AY169421	Greenland, glacier ice core sample from 3042 meters depth	99%	Alphaproteobacteria, Rhizobiales
clone Kir51gry B2.c39	insect intestine clone D	AJ459874	coleopteran larval intestine (Zophobus mori)	99%	Alphaproteobacteria, Caulobacterales
clone Kir51gry B2.c40	insect intestine clone D	AJ459874	coleopteran larval intestine (Zophobus mori)	99%	Alphaproteobacteria, Caulobacterales
clone Kir21gry B8.a29*	Janthinobacterium lividum isolate Acam	EU275366	Peru, rhizosphere soil of Acacia macracantha	99%	Betaproteobacteria, Burkholderiales
clone Kir21gry B8.b14	Xanthomonas axonopodis XV938	AF123091	Florida, plant pathogen	99%	Gammaproteobacteria, Xanthomonadales
clone Kir21gry B7.b11	Pseudomonas sp. p50	EU864269	seafloor, 2228 depth; basalt	99%	Gammaproteobacteria, Pseudomonadales
PCR Kir51gry B6-27-070104	Arvadi spring clone 17-90-ArvAB	AB425065	Switzerland, central Alps, Arvadi spring biofilm	90%	candidate division TM6
clone Kir21gry B8.a28	Australian soil Bacterium Ellin337	AF498719	Australia, Victoria, Ellinbank, grazed perennial ryegrass land soil	97%	Acidobacteria, Acidobacteriales
clone Kir51gry B4.c49	Cabo Rojo mat clone MAT-CR-H1-E11	EU245078	Puerto Rico, Cabo Rojo, hypersaline microbial mat	99%	Firmicutes, Bacillales
clone Kir51gry B4.b36	Cabo Rojo mat clone MAT-CR-H1-E11	EU245078	Puerto Rico, Cabo Rojo, hypersaline microbial mat	99%	Firmicutes, Bacillales
clone Kir51gry B2.b33	Cabo Rojo mat clone MAT-CR-H1-E11	EU245078	Puerto Rico, Cabo Rojo, hypersaline microbial mat	99%	Firmicutes, Bacillales
PCR Kir51gry B10 30-070104	Cabo Rojo mat clone MAT-CR-H1-E11	EU245078	Puerto Rico, Cabo Rojo, hypersaline microbial mat	99%	Firmicutes, Bacillales
clone Kir51gry B2.c42	Desulfonispora thiosulfatigenes DSM 11270	NR_026497	Germany, sewage plant	91%	Firmicutes, Clostridiales
clone Kir21gry B4.b5	Pontibacillus halophilus JSM 076056	EU583728	South China Sea, from sea urchin	99%	Firmicutes, Bacillales
clone Kir21gry B2.b1	Pontibacillus sp. NH11EB76	FJ232474	South China Sea, marine sediment	99%	Firmicutes, Bacillales
clone Kir21gry B2.b2*	Pontibacillus chungwhensis LS59	FJ937904	South China Sea, from marine sponge Gelliodes carnosa	99%	Firmicutes, Bacillales
clone Kir21gry B10.a6	Pontibacillus sp. CNJ912 PL04	DQ448765	Palau, marine sediment	97%	Firmicutes, Bacillales
clone Kir21gry B9.b17	Pontibacillus sp. CNJ912 PL04	DQ448765	Palau, marine sediment	99%	Firmicutes, Bacillales
clone Kir21gry B2.b3	Halobacillus trueperi GSP38	AY505522	Oklahoma, Great Salt Plains	98%	Firmicutes, Bacillales
clone Kir51gry B4.b35	Halanaerobiales bacterium Ag-C55	AB260050	Pacific, eastern flank of Juan de Fuca Ridge, rust exposed to hot fluids	92%	Firmicutes, Halanaerobiales
clone Kir21gry B9.a4	Cabo Rojo mat clone MAT-CR-P1-F04	EU246021	Puerto Rico, Cabo Rojo, hypersaline microbial mat	98%	candidate division KSB1
clone Kir21gry B9.b18	Oregon hydrate ridge clone Hyd24-32	AJ535231	Oregon, Cascadia Margin, marine sediment above hydrate ridge	89%	Bacteria, unclassified
clone Kir21gry B4.a5	Cabo Rojo mat clone MAT-CR-M7-D10	EU245868	Puerto Rico, Cabo Rojo, hypersaline microbial mat	98%	Bacteria, unclassified
clone Kir21gry B7.c12	Zodletone Spring clone Zplanct30	EF602491	Oklahoma, anaerobic, sulfide- and sulfur-rich Zodletone Spring	92%	Bacteria, unclassified
clone Kir21gry B7.b12	Gulf methane seep clone SMI1-GC205-Bac58	DQ521801	Gulf of Mexico, sediments overlying a brine pool methane seep	92%	Bacteria, Hypersaline Group II [HS-II]
clone Kir21gry B7.c13	Gulf methane seep clone SMI1-GC205-Bac58	DQ521801	Gulf of Mexico, sediments overlying a brine pool methane seep	91%	Bacteria, Hypersaline Group II [HS-II]

(Continued on next page)

47

TABLE 3

Operational taxonomic units (OTUs) retrieved from Kiritmati microbial mats and their nearest relatives with percentage identity to first match through BLASTn (*Continued*)

OTU	Nearest neighbor	Accession #	Location and habitat	Sequence similarity	Systematic position
clone Kir21gry B6.a1	Gulf methane seep clone SMI1-GC205-Bac58	DQ521801	Gulf of Mexico, sediments overlying a brine pool methane seep	92%	Bacteria, Hypersaline Group II [HS-II]
clone Kir21gry B5.b7	Cabo Rojo mat clone MAT-CR-P5-E01	EU246224	Puerto Rico, Cabo Rojo, hypersaline microbial mat	96%	Chloroflexi
clone Kir21gry B10.b8	Santa Barbara sediment clone 10bav_B12red	EU181510	Pacific, Santa Barbara Basin, sulfate-methane transition zone	93%	Planctomycetes
clone Kir21gry B6.c10	Salton Sea sediment clone SSS4A	EU592492	California, Salton Sea, hypersaline sediment	93%	Planctomycetes
PCR Kir21gry 1-070104	Guerrero Negro mat clone GN25D19A	EU731915	Mexico, Guerrero Negro, hypersaline microbial mat	94%	Crenarchaeota
clone Kir21gry c22	mud volcano clone AMSMV-S1-A61	FJ649533	Mediterranean Sea, Amsterdam Mud Volcano sapropel sediment	93%	Crenarchaeota
PCR Kir51gry 22-070104 (5) brown flocculent basis	*Methanohalophilus mahii* DSM 5219	M59133	Utah, Great Salt Lake, anaerobic sediment	97%	Euryarchaeota, Methanosarcinales
clone Kir21brw B7.34	Cabo Rojo mat clone MAT-CR-P6-E07	EU246298	Puerto Rico, Cabo Rojo, hypersaline microbial mat	97%	Alphaproteobacteria
clone Kir21brw B7.c38	*Methylobacterium fujisawaense* 1-44	AY169421	Greenland, glacier ice core sample from 3042 meters depth	99%	Alphaproteobacteria, Rhizobiales
clone Kir21brw B4.c55	insect intestine clone D	AJ459874	coleopteran larval intestine (*Zophobas mori*)	99%	Alphaproteobacteria, Caulobacterales
clone Kir21brw B4.c51	insect intestine clone D	AJ459874	coleopteran larval intestine (*Zophobas mori*)	99%	Alphaproteobacteria, Caulobacterales
clone Kir21brw B6.a16	Colorado alpine soil clone bac2nit38	EU861944	Colorado, Niwot Ridge alpine tundra soil	92%	Betaproteobacteria, Burkholderiales
clone Kir21brw B6.c29	*Pseudomonas* sp. p50	EU864269	seafloor, 2228 depth; basalt	99%	Gammaproteobacteria, Pseudomonadales
clone Kir21brw B6.c31	*Pseudomonas* sp. BSs20166	EU365518	Arctic Ocean, marine sediments	99%	Gammaproteobacteria, Pseudomonadales
clone Kir21brw B7.c37	Cabo Rojo mat clone MAT-CR-H1-E11	EU245078	Puerto Rico, Cabo Rojo, hypersaline microbial mat	99%	Firmicutes, Bacillales
clone Kir21brw B6.c33	Cabo Rojo mat clone MAT-CR-H1-E11	EU245078	Puerto Rico, Cabo Rojo, hypersaline microbial mat	99%	Firmicutes, Bacillales
PCR Kir21brw B9-19-070104	*Halobacillus* sp. CNJ915 PL04	DQ448762	Palau, marine sediment	99%	Firmicutes, Bacillales
clone Kir21brw B7.c35	Halanaerobiales bacterium Ag-C55	AB260050	Pacific, eastern flank of Juan de Fuca Ridge, rust exposed to hot fluids	92%	Firmicutes, Halanaerobiales
clone Kir21brw B6.c30	methane seep clone Eel-BE1B4	AF354145	Pacific, Cascadia subduction zone, Eel River Basin, methane seep	93%	Deltaproteobacteria
clone Kir21brw B4.a13	Cabo Rojo mat clone MAT-CR-M7-G05	EU245891	Puerto Rico, Cabo Rojo, hypersaline microbial mat	99%	Deltaproteobacteria
clone Kir21brw B7.a17	*Desulfococcus multivorans* DSM 2059	AF418173	Germany, Göttingen, sewage digester	91%	Deltaproteobacteria, Desulfobacterales

48

| clone Kir2lbrw B5.b23	Cabo Rojo mat clone MAT-CR-M2-A02	EU245470	Puerto Rico, Cabo Rojo, hypersaline microbial mat	99%	candidate division OP8
clone Kir2lbrw B5.b25	Cabo Rojo mat clone MAT-CR-H1-C02	EU245058	Puerto Rico, Cabo Rojo, hypersaline microbial mat	98%	Chloroflexi
clone Kir2lbrw B5.b24	Cabo Rojo mat clone MAT-CR-P6-G05	EU246313	Puerto Rico, Cabo Rojo, hypersaline microbial mat	97%	Chloroflexi
clone Kir2lbrw CA.c24	Cabo Rojo mat clone MAT-CR-P6-G05	EU246313	Puerto Rico, Cabo Rojo, hypersaline microbial mat	97%	Chloroflexi
clone Kir2lbrw B6.b26	Cabo Rojo mat clone MAT-CR-M1-E11	EU245434	Puerto Rico, Cabo Rojo, hypersaline microbial mat	99%	Planctomycetes
clone Kir2lbrw B7.b30	Hainan mangrove soil clone MSB-5A1	DQ811898	China, Hainan, mangrove soil	94%	Planctomycetes
clone Kir2lbrw B6.a15	Juan de Fuca Ridge clone FS142-21B-02	AY704401	Pacific, eastern flank of Juan de Fuca Ridge, oceanic basalt	94%	Planctomycetes
PCR Kir2lbrw 11-070104	Guerrero Negro mat clone GNA05C02	EU731965	Mexico, Guerrero Negro, hypersaline microbial mat	99%	Crenarchaeota
clone Kir2lbrw d64	*Methanohalophilus oregonensis* DSM 5435	NR.028237	Oregon, anoxic alkaline saline aquifer near Alkali Lake	94%	Euryarchaeota, Methanosarcinales

*Indicates partial sequence.
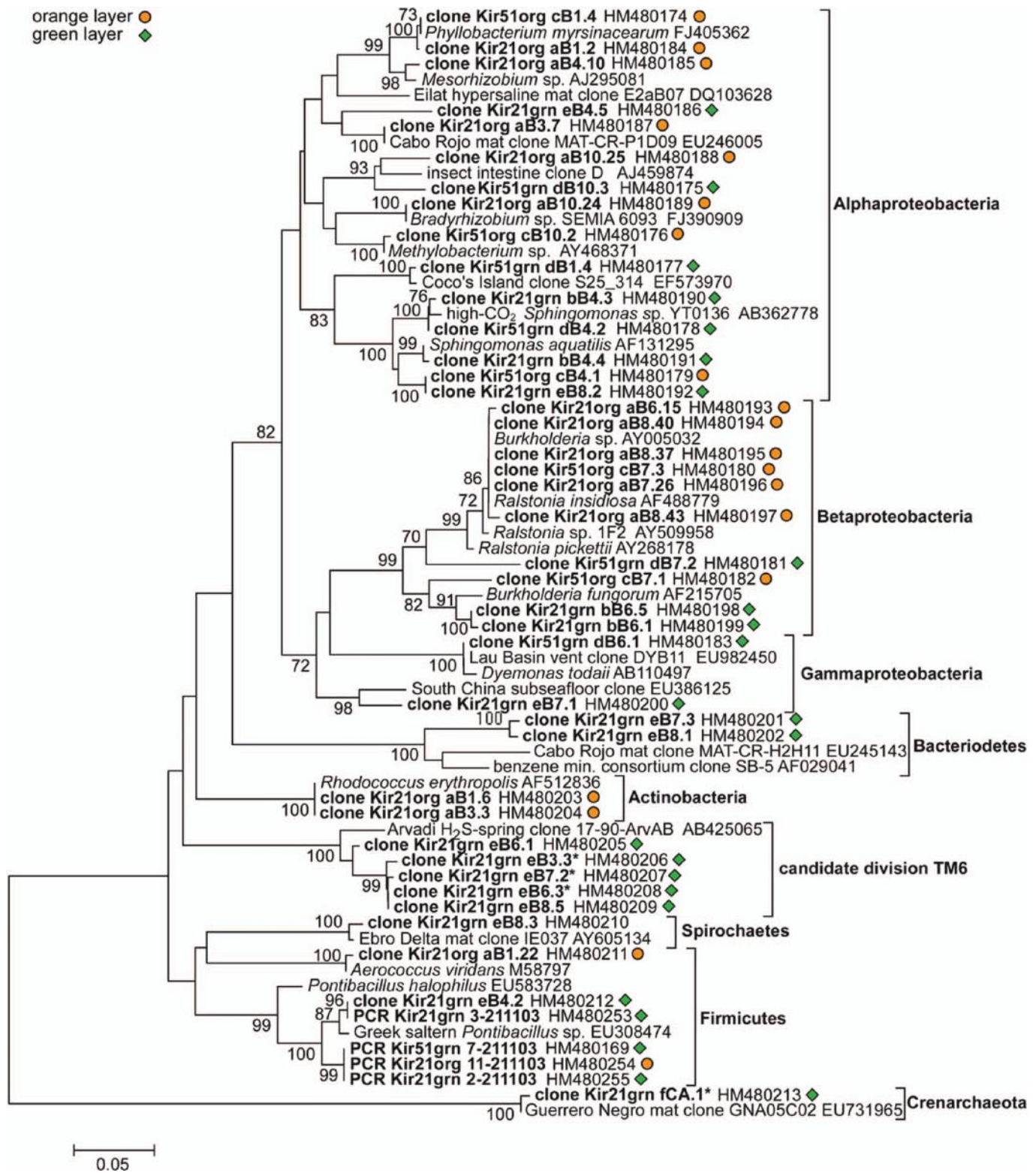
FIG. 10. Phylogenetic tree of sequences obtained from orange and green microbial mat parts, Kiritimati Lake 21 and 51, and their cultured and uncultured relatives with associated GenBank accession numbers. Bootstrap support values (percent; 1,000 replicates; only values >70% shown) are indicated at the bases of branches. The scale bar represents 5% sequence divergence (color figure available online).

FIG. 11. Phylogenetic tree of sequences obtained from purple, grey and brown microbial mat parts, Kiritimati Lake 21 and 51, and their cultured and uncultured relatives with associated GenBank accession numbers. Bootstrap support values (percent; 1,000 replicates; only values >70% shown) are indicated at the bases of branches. The scale bar represents 5% sequence divergence (color figure available online).
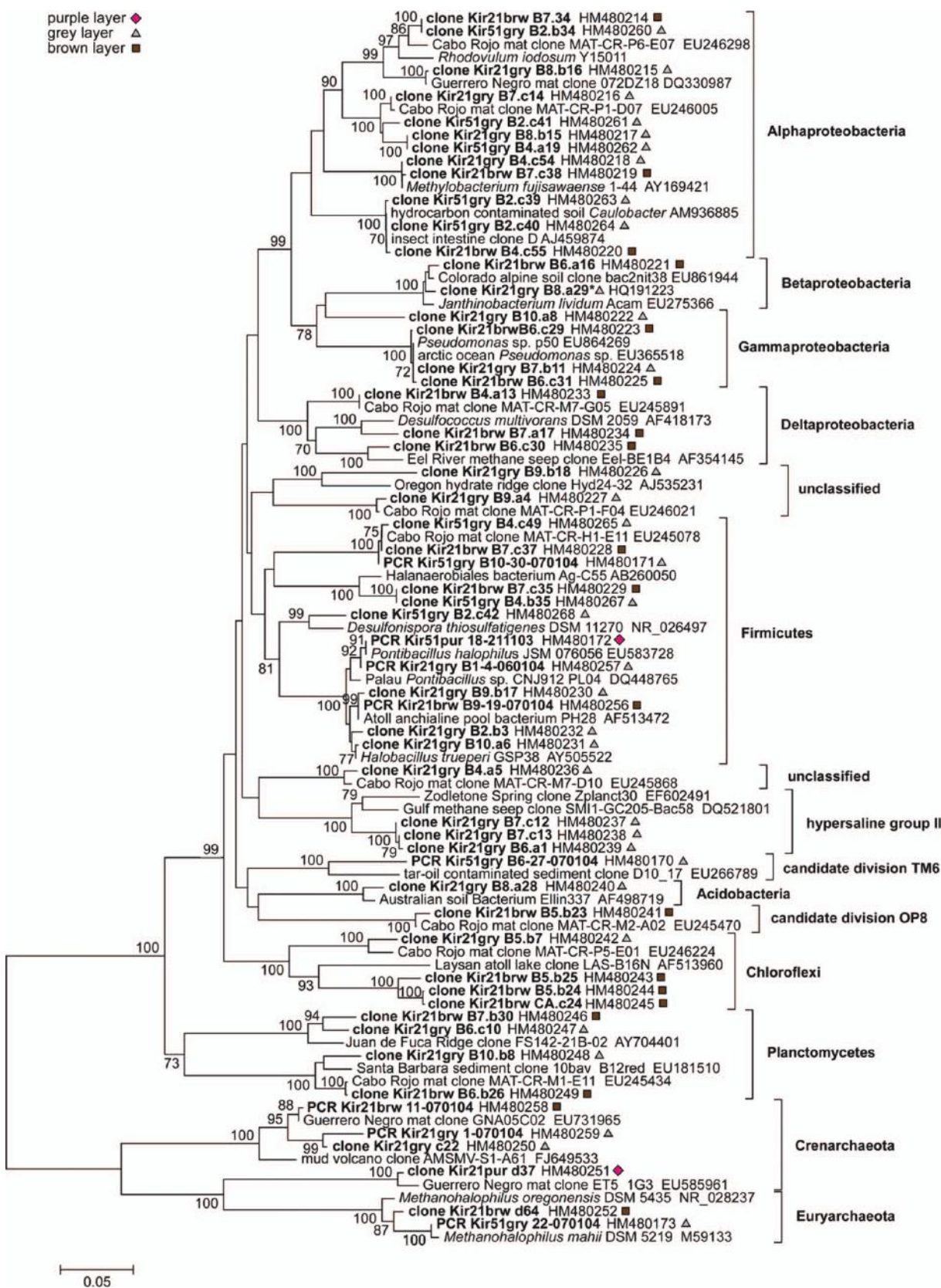
Halanaerobiales, which are halophilic anaerobes with a fermentative or homoacetogenic metabolism, has been detected.

Contrary to other layers of the Kiritimati lake 21 and 51 microbial mats, *Deltaproteobacteria* could be detected, with next relative from a Pacific Eel-River-Basin methane seep (Orphan et al. 2001) and a hypersaline microbial mat of Puerto Rico (Isenbarger et al. 2008). One clone is distantly related to *Desulfococcus multivorans* DSM 2059, a sulfate-reducing bacterium which is capable of using aromatic compounds for growth and energy generation (Widdel 1980; Peters et al. 2004). One clone assigned to the candidate division OP8 and three clones assigned to the *Chloroflexi* were found, all of them closely related (97–99% sequence similarity) to clones retrieved from a hypersaline microbial mat of Puerto Rico (Isenbarger et al. 2008).

This also applies to one *Planctomycetes* clone, while a second clone of this phylum is affiliated (94% sequence similarity) with a representative from a mid-ocean-ridge environment (Huber et al. 2006). Finally, two clones of *Archaea* have been retrieved from the brown flocculent microbial aggregates. One *Crenarchaeote* closely related (99% sequence similarity) to a clone from a Guerrero Negro hypersaline microbial mat, and one clone affiliated (94% sequence similarity) with the methanogenic Euryarchaeote *Methanohalophilus oregonensis* DSM 5435. Similar to the *Methanohalophilus* strains mentioned from the grey layer, this stain grows on methyl compounds, but not on H_2 and CO_2, formate, or acetate, an observation that applies to methanogens in other hypersaline, sulfate-containing anoxic environments (Liu et al. 1990).

Hydrochemical Gradients Across Microbial Mats

Physicochemical gradients detected by standard field electrodes at Lake 21 are shown in Figure 12. Only data for daylight conditions are available. Conductivity measurements document a decline in salinity from the water column through the mat to pore water. Temperature reaches a maximum within photosynthetic mat parts, due to light adsorption. The pH increases from water column (8.27) at the orange top layer of the mat to a maximum value of 8.90. Within the mat, a decline to 8.60 (green layer) and finally 7.60 (grey mat basis) is observed, while in the pore water near-neutral pH was measured (7.16). Similar to pH, pε (negative log of the electron activity) increases from water column (+2.84) to a maximum value of in the orange top layer (+3.25) of the mat, then declines to +1.69 in deeper mat parts. Negative values were obtained from the mat basis (−2.10) and the pore water below the mat (−2.62).

Data of cation and anion concentrations are only available from the water column and from the pore water in the microbialite below the mats (Table 2). Based on these data, aragonite saturation is very high in the water column, whereas in pore water shows only saturation to slight supersaturation (Figure 12). Alkalinity is the same above and below the mats. Ca^{2+} concentration is lower in the pore water, which, however, reflects decreased salinities (Figure 12). For Lake 22, pore water is much lower in Ca^{2+} if compared to the water column, but

fits well to the calculated pathway of evaporation and mineral precipitation (Figure 4). Low SI_{Arag} values of the pore water below the mats therefore largely reflect a high PCO_2 and hence decrease pH (Figure 12). This coincides with high ammonium concentration, increased phosphate and dissolved iron (Table 2).

Fabric and Composition of Microbial Carbonate

Initial precipitates. Initial mineral precipitates within the microbial mats comprise three different types: (i) spherulites, (ii) streaks of aragonite needles, and (iii) gypsum crystals.

(i) Spherulites develop from initial microcrystalline (<1 μm) aggregates, with up to 50 μm in size. XRD analysis and high Sr concentrations detected by EPMA indicate an aragonite mineralogy. These patchy small aggregates already occur 0.75 below top of mat, and serve as nuclei for radial-fibrous veneers by aragonite needles which finally result in large spherulites 1–2 mm in size. Well developed spherulites are observed in lower half of the orange layer (e.g., 15 mm below top to the mat; Figure 8A), and accumulate in the green layer by condensation of the exopolymer mat matrix.

(ii) Streaks of aragonite needles form in crevice-like zones of the exopolymer framework of the mat. These aragonite needle streaks occur first within basal parts of the green mat layer and, more intensively developed, within the purple layer of the mat (Figures 8A, H). XRD analysis and high Sr concentrations detected by EPMA indicate an aragonite mineralogy for these 2–3 μm wide and 10–20 μm long needles. In addition, isometric $CaCO_3$ crystals less than 1 μm in size occur. Within larger aggregates, the crystals become pseudohexagonal and up to 10 μm size.

(iii) Scattered gypsum crystals occur within the exopolymer matrix through the microbial mat. First monocline crystals and twins of 15 × 50 μm size are visible already near the top of the mats. XRD analysis of freeze-dried mat samples (orange, green and grey layers) indicated gypsum and halite besides of aragonite. In addition, traces of bischofite have been detected in the grey mat basis of Lake 51.

Microbialite. The resulting microbialite, as observed below mats containing the initial precipitates described above, is characterized by a reticulate framework composed of three structural elements (Figures 13A, B, C): (i) Vertical, jagged carbonate sheets and threads 0.25–1 mm thick with comb-like arrangement, forming 1–4 cm high layers, (ii) subhorizontal irregular, porous-friable carbonate layers of approximately 3–6 mm thickness, and (iii) gypsum crystal layers up to 5 cm thickness. The "reticulate microbialite" in Kiritmati lakes therefore differs from other microbial carbonates denominated by the same term (e.g., Pratt 1982; Kahle 1994; Parcell 2002), but composed of clotted micrite or microbial peloids.
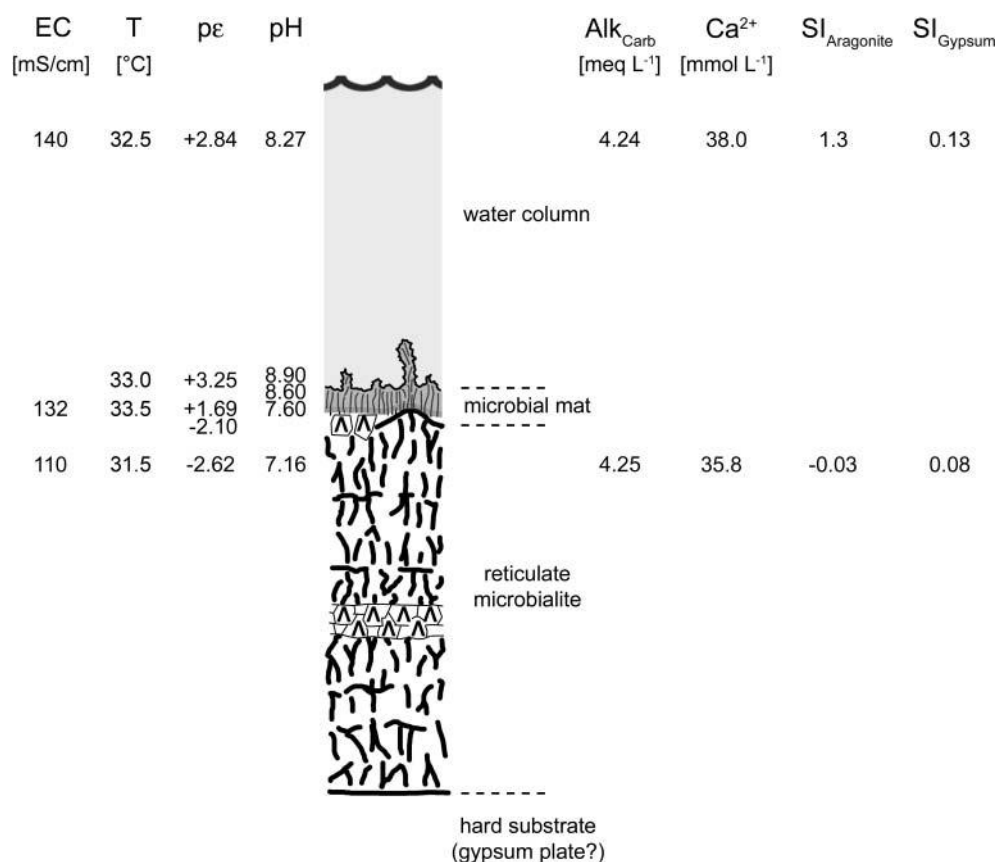
FIG. 12. Physicochemical and hydrochemical gradients across the microbial mat in Lake 21, between dig #2 and #3, under daylight condition (04.09.2002).

(i) Vertical aragonite sheets commonly show a microspar-like central zone pervaded by microcrystalline stripes (Figures 13C, D). These central parts are composed of interlocking, 4–30 μm sized aragonite crystals with pseudohexagonal habitus and dark organic inclusions (Figure 13D). The central zone is enclosed by a microcrystalline marginal zone. Finally aragonite botryoids grade into fibrous veneers, which form the last phase (Figure 13D).

(ii) Subhorizontal, friable layers consist of interlocking aragonite crystals, too. The layers commonly exhibit dark-brown to black dots in central layer parts, which turned out in microscopy as fossilized colonies of coccoid cyanobacteria (*Gloeocapsa* morphotype; Figure 13E). In top view, subhorizontal layers of Lake 22 commonly show bubble-like voids. Associated with the subhorizontal layers are aragonitic spherulites of 100–500 μm diameter occur. Much larger are spherulites in Lake 2 microbial mats, which attain up to 2 mm in diameter (Figure 14). They form friable carbonate sand attached to the subhorizontal layers, but occur scattered throughout the mat and enclosed in microbialite sheets as well. In one of the subhorizontal, dense layer of aragonite in Lake 2, parallel to fan-like arranged erect cyanobacterial filament traces (4–6 μm diameter, dark-brownish envelope, internally aragonitic)

have been observed. Here, aragonite is composed of 4–20 μm large interlocking crystals, i.e., microcrystalline to microsparitic. Locally, fibrous smooth aragonite veneers line closed voids, and thin fibrous aragonite needles grow on spherulites and irregular laminae surfaces.

(iii) Restricted to a few horizons, e.g. 30 cm below microbialite top in digs #3 and #4, idiomorphic gypsum crystals up to 5 mm in size form horizontal levels (Figure 13F). Starting with scattered aggregates attached to microbialite sheets, these crystals fuse to coalescent layers 2 cm thick (Figure 13A). Also, the solid substrate below the microbialite is formed by coarse crystalline gypsum.

XRD analysis and EPMA measurements demonstrate that microbialites are composed of aragonite (Figure 14). Sr concentrations in aragonitic microbialites, spherulites and fibrous aragonite cements are high, with aragonite of Lake 2 having comparatively low values (Figure 15).

With respect to Mg in the aragonite, concentrations vary between 150 and 1500 ppm, with one exception of 2100 ppm. No systematic relations, e.g. between central parts of layers and fibrous veneers, were recognized. Mg-calcite is restricted to small patches and seams in microbialites cementing aragonitic spherulites of Lake 2, and miliolid foraminiferal tests in pore
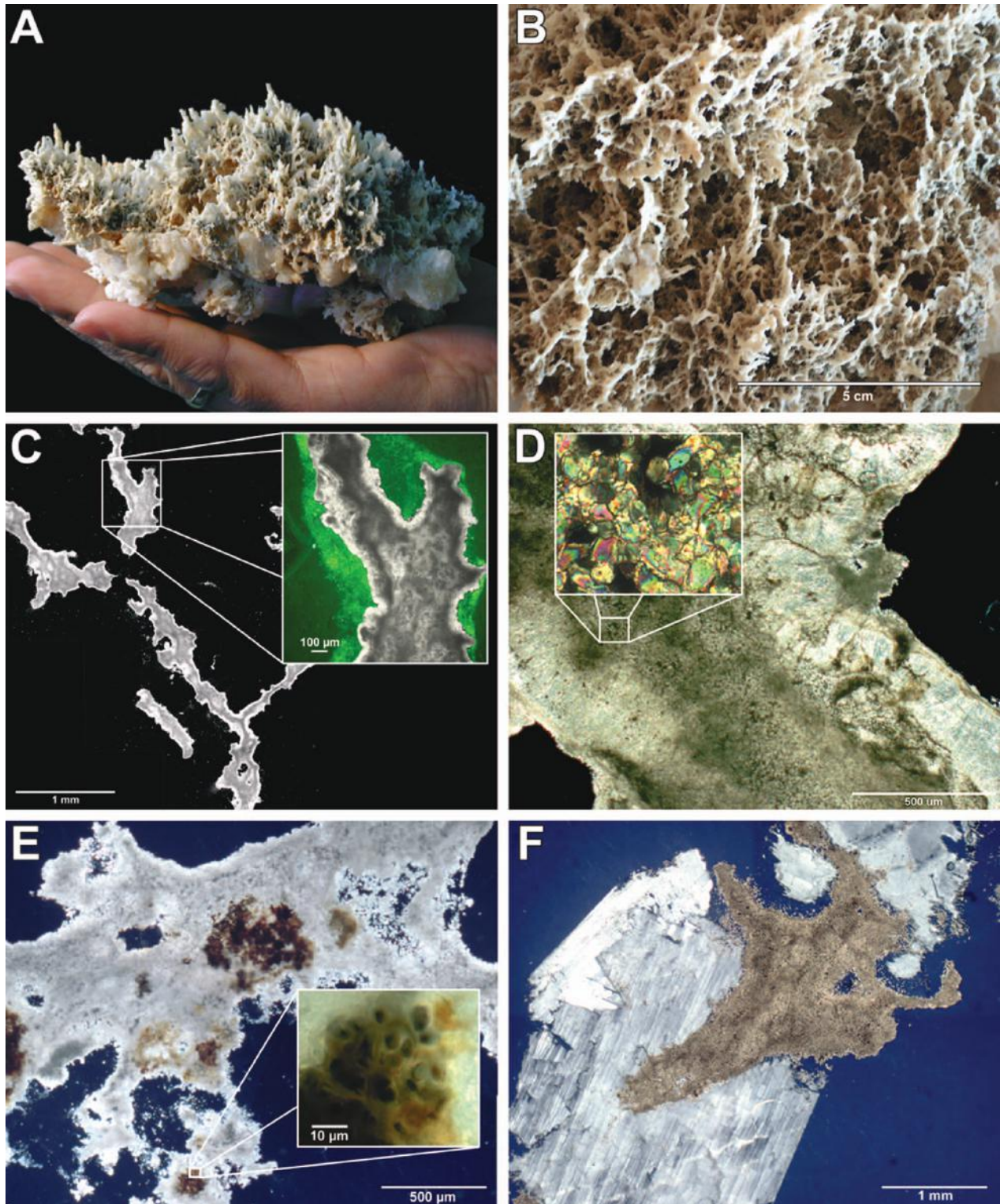
FIG. 13.   Fabric and composition of microbialites. A. Specimen of a reticulate microbialite from Lake 21, dig #3 / 3a. Note white gypsum crystals at bottom of sample. B. Same specimen in top view. C. Thin section of vertical aragonite sheets showing a microsparitic aragonite central zone, a microcrystalline marginal zone, and a fibrous aragonite veneers. Biofilm veneers (brownish flocculent aggregates) occur only in top parts of the microbialite. X Nicols. Insert: overlay of X Nicols view and fluorescence micrograph; excitation 400–440 nm; emission >570 nm. Lake 21, sample dig 5 / 5a. D. Detail of vertical sheet of microbialite, with fibrous aragonite veneer. Insert: Microspar-sized pseudohexagonal aragonite in central parts of the sheet. X Nicols. Lake 21 dig 3 / 3a. E. Horizontal layer of aragonite, with remains of coccoid cyanobacteria (insert). Plane polarized light. Lake 21 dig 3 / 3a. F. Gypsum crystals growing on aragonitic reticulate microbialite of Lake 21, dig 3 / 3a. Plane polarized light.
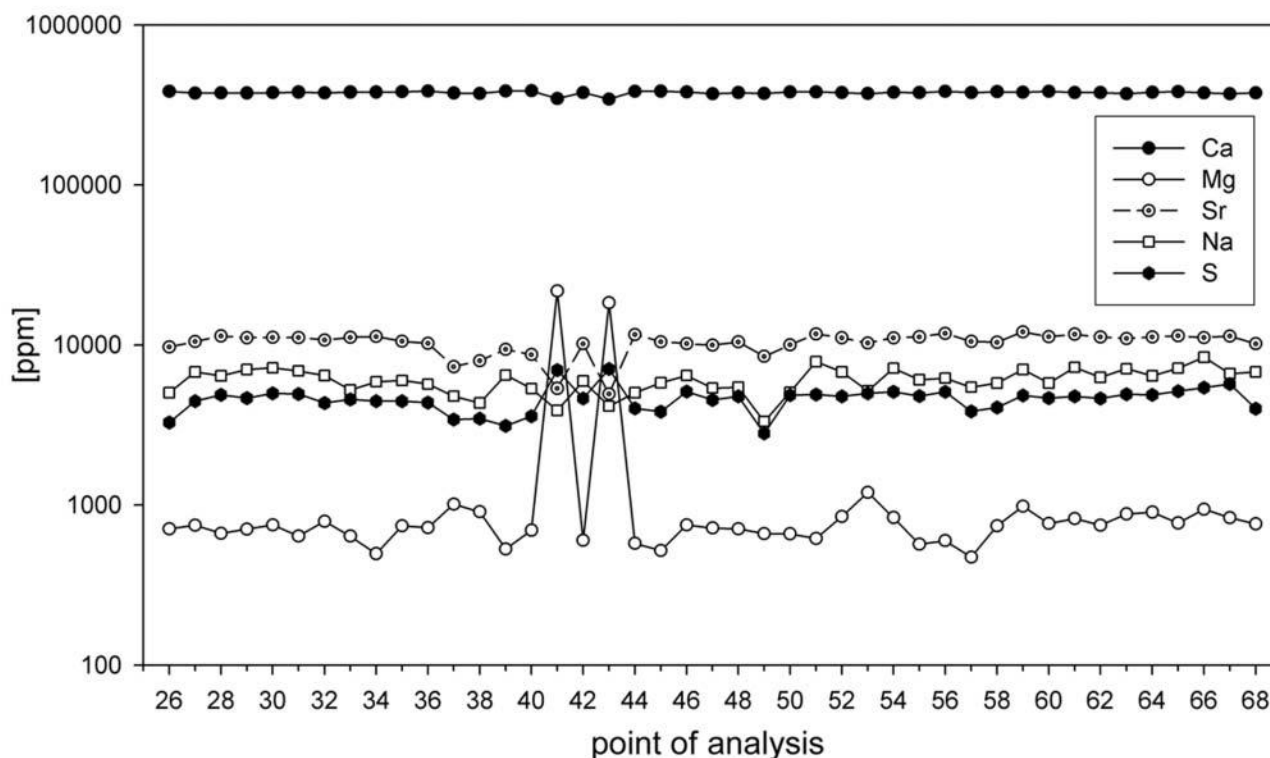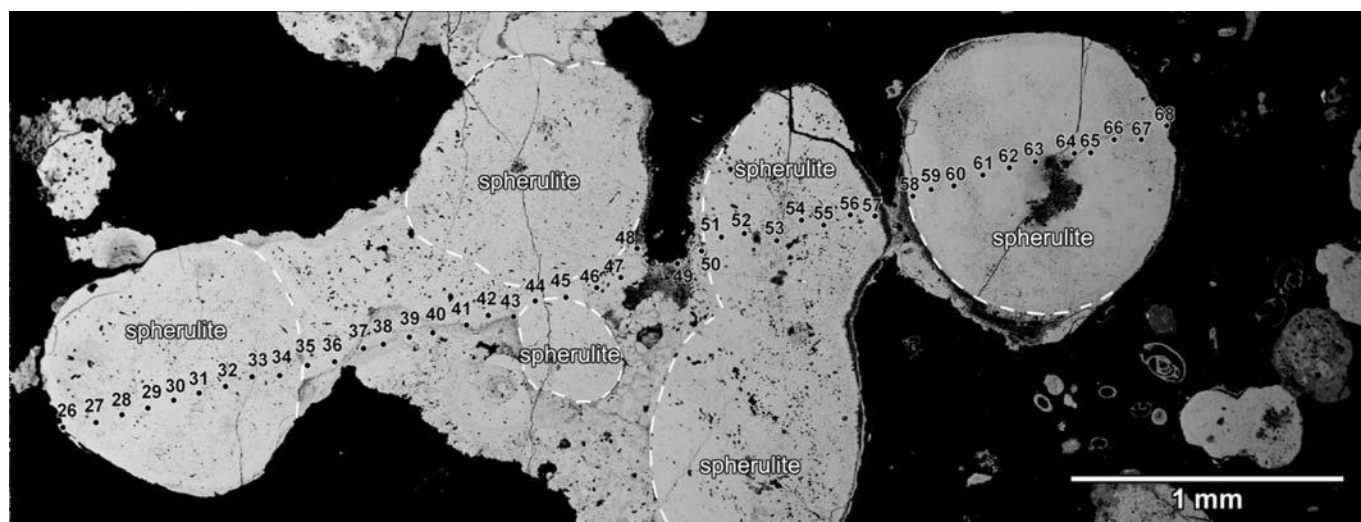
FIG. 14.   Top: Back-scatter electron micrograph of a spherulite-rich microbialite layer of Lake 2, dig #2, with aragonitic components appearing white, and Mg-containing calcium carbonate appearing darker. Outline of spherulites is indicated by white dashed lines. Note miliolid foraminiferal tests in pore space of the microbialite. Bottom: Electron microprobe traverse of Ca, Mg, Sr, Na and S demonstrating an aragonitic composition of the microbialite with only traces of Mg-calcite (spots 41 and 43).

spaces of the microbialites in Lake 2 and 21 (Figure 14). Fe and Mn concentrations are at or below detection limits. Iron sulfides have not been detected, neither by EMPA nor XRD analysis.

Stable Carbon and Oxygen Isotopes

Stable carbon and oxygen isotopes have been analyzed from lacustrine and lagoonal microbialites, including Recent as well

as subfossil to Holocene precipitates. For comparative purposes, Recent as well as Holocene-subfossil skeletal carbonates have been analyzed, too (Table 4, Figure 16).

For the marine and marine-lagoonal skeletal carbonates, i.e., Holocene reef debris of a drill core at Decca (Figure 1), subfossil shells and corals from vicinity of lakes, and Recent agglutinated oncoids from the lagoon at London (Figure 1), values range from
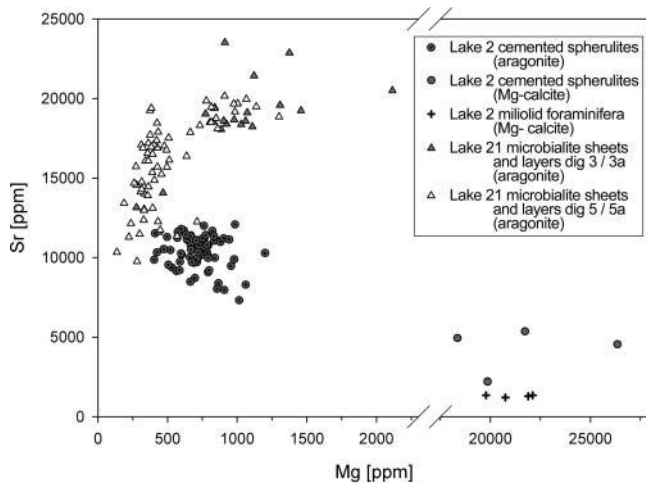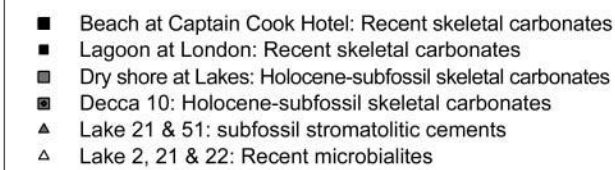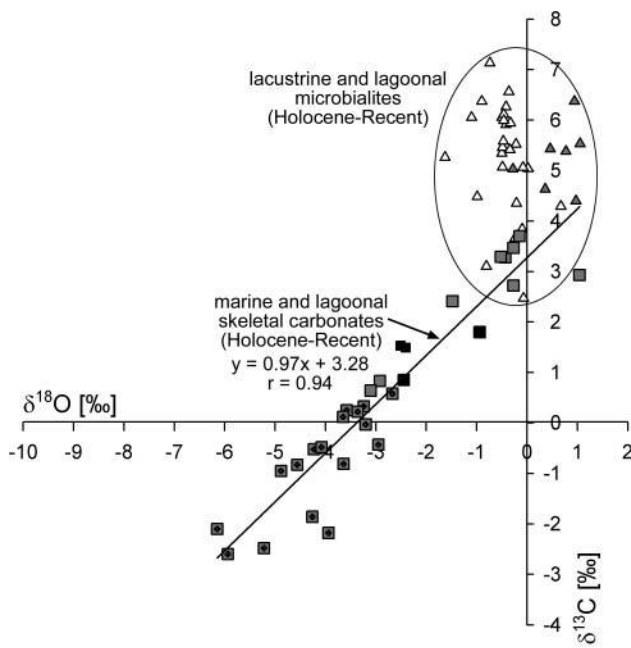
FIG. 15.   Cross-plot of Mg and Sr concentrations in Lake 2 and 21 micro-bialites, measured by electron microprobe.

$-2.6‰ \, \delta^{13}C$ and $-6.2‰ \, \delta^{18}O$ to $+3.7‰ \, \delta^{13}C$ and $+1.0‰ \, \delta^{18}O$. A clear covariation of $\delta^{13}C$ and $\delta^{18}O$ with $r = 0.94$ is evident for these carbonates (Figure 16A). In contrast to this, subfossil stromatolitic cements deviate from this trend by increased $\delta^{13}C$.

Here, no covariation of stable carbon and oxygen isotope values is evident. Likewise, all Recent microbialitic carbonates of Lake 2, 21 and 22 are significantly enriched in ^{13}C, if compared to the marine-lagoonal skeletal carbonates (Figure 16A).

Within the microbialite-hosting hypersaline lakes distinct variations in $\delta^{13}C$ at similar $\delta^{18}O$ are evident (Figure 16B): Most positive values were obtained from spherulites ($+5.1$ to $+7.1‰$ $\delta^{13}C$) and a horizontal layer with cyanobacterial filament traces ($+6.0‰ \, \delta^{13}C$). In contrast, vertical sheets and horizontal layers range from values similar to that of the cyanobacterial layer in Lake 2 ($+6.3‰ \, \delta^{13}C$) to significantly less ^{13}C enriched ratios ($+2.5‰ \, \delta^{13}C$) (Figure 16B).

INTERPRETATION: HABITAT, MICROORGANISMS AND MICROBIALITE FORMATION

Microbialite formation in the investigated Lakes 2, 21, and 22 currently takes place, as indicated by delicate needles of arago-nite within the exopolymer matrix of their microbial mats. The mode of precipitation, however, in this actively growing micro-bialite system seems to be peculiar. Despite of high aragonite supersaturation in the water column and high photosynthetic activity, only minor $CaCO_3$ precipitates are observed in the top
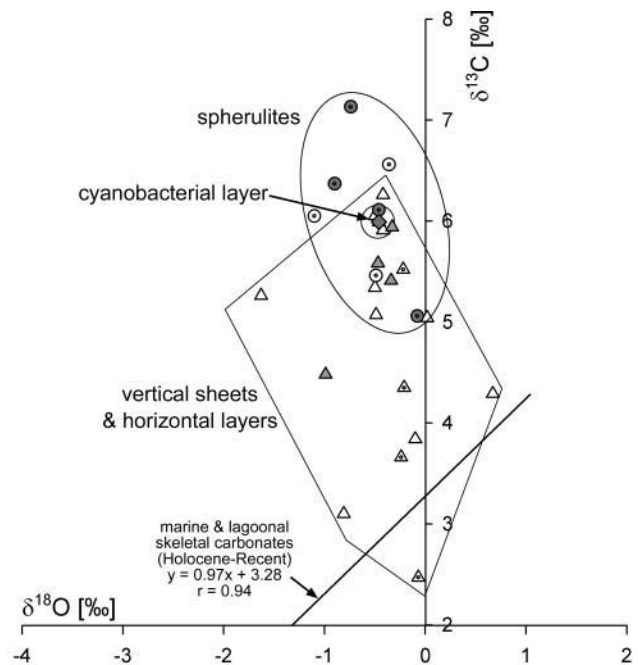

FIG. 16.   Stable carbon and oxygen isotope values of Recent and Holocene-subfossil carbonates of Kiritimati. A. Cross-plot of $\delta^{13}C$ versus $\delta^{18}O$ of Holocene to Recent skeletal carbonates and microbialites. B. Variations of $\delta^{13}C$ and $\delta^{18}O$ of microbialites components within the hypersaline Lakes 2, 21, and 22.

TABLE 4

Stable carbon and oxygen isotopes of skeletal and microbial carbonates of Kiritimati

Sample	Location	Description	$\delta^{13}C$ [‰ V-PDB]	σ	$\delta^{18}O$ [‰ V-PDB]	σ
	Recent marine skeletal carbonates					
Kir 60	Beach at Captain Cook Hotel	echinoid spine, Mg-calcite	1.80	0.02	−0.94	0.03
Kir 61	Beach at Captain Cook Hotel	*Halimeda*-segment, aragonite	0.85	0.02	−2.45	0.03
	Recent marine-lagoonal skeletal carbonates					
Kir 63	Lagoon at London	carbonate sand of oncoid core, aragonite and Mg-calcite	1.53	0.02	−2.51	0.02
Kir 64	Lagoon at London	agglutinated carbonate sand of oncoid cortex, aragonite and Mg-calcite	1.49	0.02	−2.41	0.03
	Recent microbialites of hypersaline lakes					
Kir 30	Lake 21: Dig 2a	white vertical jagged microbialite sheet, aragonite	5.04	0.01	0.02	0.03
Kir 31	Lake 21: Dig 2a	white porous horizontal microbialite layer, aragonite	5.52	0.01	−0.22	0.01
Kir 32	Lake 21: Dig 2a	grey-black layer in white dendritic microbialite sheet, aragonite	4.29	0.01	0.67	0.01
Kir 33	Lake 21: Dig 2b	mm-sized white spherulites from horizontal friable microbialite layer, aragonite	5.46	0.02	−0.49	0.03
Kir 34	Lake 21: Dig 2b	poorly lithified, horizontal friable microbialite layer composed of fine-grained spherulites, aragonite	2.47	0.02	−0.07	0.04
Kir 35	Lake 21: Dig 2b	white porous horizontal microbialite layer with few spherulites, aragonite	6.56	0.02	−0.36	0.02
Kir 36	Lake 21: Dig 2d	white dense horizontal microbialite layer, aragonite	3.66	0.02	−0.24	0.03
Kir 37	Lake 21: Dig 2d	white vertical jagged microbialite sheet grown upside on horizontal layer, aragonite	6.05	0.02	−0.50	0.03
Kir 38	Lake 21: Dig 3a	white vertical jagged microbialite sheet, aragonite	5.91	0.01	−0.42	0.02
Kir 39	Lake 21: Dig 3a	white to grey porous horizontal microbialite layer, aragonite	4.35	0.02	−0.21	0.01
Kir 40	Lake 21: Dig 3a	white vertical jagged microbialite sheet, aragonite	3.84	0.02	−0.10	0.04
Kir 41	Lake 21: Dig 3b	white vertical jagged microbialite sheet, aragonite	6.26	0.01	−0.42	0.03
Kir 42	Lake 21: Dig 4a	white vertical jagged microbialite sheet, aragonite	5.26	0.02	−1.63	0.03
Kir 43	Lake 21: Dig 4c	white vertical jagged microbialite sheet, aragonite	5.07	0.02	−0.49	0.03
Kir 44	Lake 21: Dig 4b	white vertical jagged microbialite sheet, aragonite	5.34	0.03	−0.50	0.03
Kir 45	Lake 21: Dig 4b	pale-orange friable spherulitic microbialite layer at contact to mat basis, aragonite	6.05	0.01	−1.10	0.01
Kir 46	Lake 21: Dig 5a	white vertical jagged microbialite sheet, aragonite	3.10	0.01	−0.81	0.03
Kir 47	Lake 22: Dig 1	white porous horizontal microbialite layer with spherulites, aragonite	5.58	0.03	−0.47	0.03
Kir 48	Lake 22: Dig 1	white horizontal layer 5 mm below microbialite top with cyanobacterial filament traces, aragonite	5.99	0.01	−0.46	0.03
Kir 49	Lake 22: Dig 2a	white horizontal and vertical jagged microbialite sheets, aragonite	5.41	0.03	−0.34	0.02
Kir 50	Lake 22: dry shore	white porous horizontal microbialite shingle with vesicular fabric, aragonite	5.94	0.02	−0.33	0.03
Kir 51	Lake 22: Dig 3a	white porous horizontal microbialite layer with few spherulites, aragonite	4.48	0.01	−0.99	0.02
Kir 52	Lake 2: Dig 2a+b	mm-sized white spherulites from orange-brown microbial mat, aragonite	6.37	0.02	−0.90	0.03
Kir 53	Lake 2: Dig 2a+b	white horizontal microbialite layer, aragonite	6.11	0.03	−0.46	0.03
Kir 54	Lake 2: Dig 2a	white horizontal microbialite layer with spherulites, aragonite	5.06	0.01	−0.08	0.04

(Continued on next page)

TABLE 4

Stable carbon and oxygen isotopes of skeletal and microbial carbonates of Kiritimati *(Continued)*

Sample	Location	Description	$\delta^{13}C$ [‰ V-PDB]	σ	$\delta^{18}O$ [‰ V-PDB]	σ
Kir 55	Lake 2: Dig 2a	mm-sized white spherulites from orange-brown microbial mat, aragonite	7.13	0.03	−0.74	0.02
	Holocene-subfossil marine-lagoonal skeletal carbonates					
Kir 56	Lake 21: *Acropora*-gravel with marine molluscs	white-grey carbonate sand, aragonite and Mg-calcite	0.83	0.02	−2.92	0.04
Kir 57	Lake 21: *Acropora*-gravel with marine molluscs	oister shell, calcite	3.70	0.01	−0.15	0.02
Kir 58	Lake 21: *Acropora*-gravel with marine molluscs	*Acropora*-branch, aragonite	0.64	0.02	−3.10	0.03
Kir 59	Lake 51: subfossil coquina of dry shore	oister shell, calcite	3.28	0.02	−0.43	0.03
Kir 18	Lake 51: subfossil tepee crust	orange-brown gastropod shell ("*Cerithium*"), aragonite	2.41	0.03	−1.48	0.02
Kir 22	Lake 51: fossil oister limestone bed (upper bed)	bioclastic microcrystalline carbonate between oister shells, aragonite and Mg-calcite	3.47	0.02	−0.27	0.02
Kir 23	Lake 51: fossil oister limestone bed (upper bed)	oister shell, calcite	3.29	0.01	−0.52	0.02
Kir 24	Lake 51: fossil oister limestone bed (lower bed)	oister shell, calcite	2.72	0.01	−0.27	0.01
Kir 26	Lake 21: lithified subfossil microbialite-oister bed	oister shell, calcite	2.93	0.02	1.04	0.02
	Holocene-subfossil marine-lagoonal microbialites					
Kir 19	Lake 51: subfossil tepee crust	undulating, upwards-growing stromatolitic crust, fibrous aragonite	5.53	0.03	1.05	0.03
Kir 20	Lake 51: subfossil tepee crust	fibrous cement from inside of gastropod shell, aragonite	4.63	0.03	0.36	0.02
Kir 21	Lake 51: subfossil tepee crust	thin stromatolitic shingle ("chip") from cemented top of tepee crust, aragonite	5.03	0.03	−0.28	0.03
Kir 25	Lake 51: fossil oister limestone bed (lower bed)	digitate, upwards-growing stromatolitic carbonate from top of oister limestone bed, aragonite	5.43	0.01	0.46	0.03
Kir 27	Lake 21: lithified subfossil microbialite-oister bed	fibrous stromatolitic cement, aragonite	6.37	0.01	0.94	0.02
Kir 28	Lake 21: lithified subfossil microbialite-oister bed	fibrous stromatolitic cement, aragonite	5.38	0.02	0.77	0.01
Kir 29	Lake 21: lithified subfossil microbialite-oister bed	fibrous stromatolitic cement from inside of gastropod shell, aragonite	4.40	0.01	0.97	0.02
	Holocene marine skeletal carbonates					
Kir 1	monitoring well Decca: 3.7 m depth	coralline red-algal skeleton, Mg-calcite	−2.18	0.03	−3.94	0.03
Kir 2	monitoring well Decca: 3.7 m depth	bioclastic rudstone: molluscs, foraminifera, red-algae, echinoderms, corals, microcrystalline matrix	0.58	0.01	−2.67	0.02
Kir 3	monitoring well Decca: 4.7 m depth	coralline red-algal skeleton, Mg-calcite	−2.48	0.01	−5.22	0.04
Kir 4	monitoring well Decca: 4.7 m depth	coral skeleton, aragonite	0.25	0.02	−3.58	0.03
Kir 5	monitoring well Decca: 4.7 m depth	bioclastic rudstone: molluscs, foraminifera, red-algae, echinoderms, corals, microcrystalline matrix	0.33	0.02	−3.24	0.03

TABLE 4
Stable carbon and oxygen isotopes of skeletal and microbial carbonates of Kiritimati *(Continued)*

Sample	Location	Description	$\delta^{13}C$ [‰ V-PDB]	σ	$\delta^{18}O$ [‰ V-PDB]	σ
Kir 6	monitoring well Decca: 5.3 m depth	coralline red-algal skeleton, Mg-calcite	−2.60	0.02	−5.94	0.03
Kir 7	monitoring well Decca: 5.3 m depth	bioclastic rudstone: molluscs, foraminifera, red-algae, echinoderms, corals, microcrystalline matrix	0.22	0.02	−3.36	0.03
Kir 8	monitoring well Decca: 5.55 m depth	coralline red-algal skeleton, Mg-calcite	−0.52	0.01	−4.23	0.02
Kir 9	monitoring well Decca: 5.55 m depth	bioclastic rudstone: molluscs, foraminifera, red-algae, echinoderms, corals, microcrystalline matrix	0.12	0.01	−3.65	0.04
Kir 10	monitoring well Decca: 5.55 m depth	echinoid spine, Mg-calcite	−0.03	0.02	−3.20	0.02
Kir 11	monitoring well Decca: 5.8 m depth	coralline red-algal skeleton, Mg-calcite	−2.10	0.02	−6.15	0.04
Kir 12	monitoring well Decca: 5.8 m depth	bioclastic rudstone: molluscs, foraminifera, red-algae, echinoderms, corals, microcrystalline matrix	−0.48	0.02	−4.08	0.02
Kir 13	monitoring well Decca: 5.8 m depth	echinoid spine, Mg-calcite	−0.81	0.01	−3.64	0.03
Kir 14	monitoring well Decca: 6.1 m depth	coralline red-algal skeleton, Mg-calcite	−0.95	0.02	−4.88	0.04
Kir 15	monitoring well Decca: 6.1 m depth	coral skeleton, aragonite	−1.86	0.01	−4.26	0.02
Kir 16	monitoring well Decca: 6.1 m depth	echinoid spine, Mg-calcite	−0.43	0.01	−2.95	0.03
Kir 17	monitoring well Decca: 6.1 m depth	bioclastic rudstone: molluscs, foraminifera, red-algae, echinoderms, corals, microcrystalline matrix	−0.83	0.01	−4.56	0.02
Kir 62	shallow pit close to Lake 52: fossil carbonate sand	coralline red-algal skeleton (rhodoid), Mg-calcite	−2.38	0.01	−2.74	0.03

parts of the microbial mat of hypersaline lakes on Kiritimati. Instead, $CaCO_3$ precipitates occur more excessively in lower mat parts at the transition to the anoxic zone. This observation leads to the hypothesis that exopolymer degradation and breakdown of inhibition may play a crucial role in the formation of these microbialites characterized by an enigmatic reticulate fabric. Indeed, a crucial role of exopolymers in calcium carbonate precipitation in these mats has previously been proposed by Défarge et al. (1996).

From hydrochemical point of view, the habitat of the microbialite-forming mats generally can be described as evaporated seawater. These hypersaline lake waters are highly supersaturated with respect to aragonite ($SI_{Arag} = 1.0$ to 1.3), and no significant differences in aragonite supersaturation between the microbialite-containing lakes 2, 21, 22 and the microbialite-free lake 51 (Manulu Lagoon) are obvious (Table 2, Figures 5A, B). However, microbialite-forming lakes 2, 21, and 22 have higher Ca^{2+} than expected by simple evaporation and aragonite plus gypsum precipitation pathway from marine waters, while Lake 51 (Manulu Lagoon) fits to the pathway (Figure 4B). Hence, an additional surface or groundwater influx of Ca^{2+} dissolved from Holocene carbonates to the microbialite-containing lakes

2, 21 and 22 is suggested. With respect to nutrients, the aerobic lake water column is low in NH_4^+ and PO_4^{3-}, while the anoxic pore waters below the mats show high NH_4^+ at only slightly increased PO_4^{3-} concentrations.

The prokaryotic community certainly reflects these habitat conditions (Table 3), although a definitive proof of functional relationships cannot be made on basis of 16S rDNA analysis. Apart from the *Cyanobacteria*, which are the major primary producers, a high number of clones of other phototrophs (purple non-sulphur bacteria, *Chloroflexi*) and non-phototrophs retrieved from the Kiritimati microbial mats find their closest, commonly halotolerant, relatives in other microbial mats of hypersaline settings, particularly of the lagoon at Cabo Rojo, Puerto Rico (Isenbarger et al. 2008) and Guerrero Negro (Orphan et al. 2008; Robertson et al. 2009).

Also, phototrophic mat parts contain aerobic chemoorganotrophs, some of them with preference to oligotrophic habitats (*Caulobacterales* and *Sphingomonadales*). Finally, the genera *Burkholderia* and *Ralstonia* (both aerobic taxa which include animal and plant pathogens but also plant symbionts) as well as soil-inhabiting bacteria point to a potential surface (plant detritus) or subsurface influx (groundwaters) from terrestrial

areas. Surface influx of organic material may also be indicated by chitinase-producing phylotypes (*Janthinobacterium lividum*; Gleave et al. 1995), which is in accordance with the presence of insect remains within the mats (Figure 8I).

Strikingly, a number of clones from the investigated microbial mats show closest relatives to microorganisms either involved in methane production (i.e., methanogenic *Archaea*) or consumption of methane or methyl compounds (e.g., *Methylobacterium populi*; Van Aken et al. 2004) or hydrocarbons (e.g., certain taxa of candidate phylum TM6; Winderl et al. 2009). Specifically, close relatives come from methanotrophic communities of seep brine pools (Hypersaline group II; Lloyd et al. 2006), Mediterranean mud volcanoes or methane seeps off the coast of North America (Lanoil et al. 2001; Orphan et al. 2001). Methanogens, represented by the genus *Methanohalophilus*, appear to be one of the dominant organisms in anaerobic mat parts. All this points to a significant role of methane and methyl components in the carbon cycle of the microbial mats.

In addition, aerobic as well as anaerobic mat parts contain representatives that potentially metabolize aromatic compounds (e.g., benzene; by *Rhodococcus erythropolis*; e.g. Fahy et al. 2008). Most likely, these organisms metabolize other organic compounds naturally occurring within the mats, but a possible anthropogenic contamination by fuel or coal tar from the former military use of the atoll cannot be excluded.

The presence of sulphate-reducing bacteria (SRB) appears to be more difficult to assess. Specific biomarkers (C_{17} PLFAs) substantiate the presence of oxygen-tolerant sulphate-reducers in the top layer of the mats on Kiritimati (Büring et al. 2009). Nonetheless, the available clone sequence data from Kiritimati indicate *Deltaproteobacteria* only for the grey and brown-flocculent anoxic mat parts, where H_2S indeed is present although iron sulfide precipitation lacks due to low availability of iron. In the green layer, our study reveals instead representatives of the candidate division TM6, which is phylogenetically affiliated with the *Deltaproteobacteria*. In any case, experiments with ^{35}S-labeled sulfate as well as fluorescence *in situ* hybridizations indicate the presence and activity of O_2-tolerant SRB in aerobic microbial mats parts of similar habitats (Guerrero Negro; Canfield & Des Marais 1991; Risatti et al. 1994; Minz et al. 1999).

Physicochemical and hydrochemical gradients across the Kiritimati microbial mats, although available only for daylight conditions, demonstrate a high impact of oxygenic photosynthesis in upper mat parts (Figure 12), a process that potentially drives $CaCO_3$ precipitation (Bissett et al. 2008; Shiraishi et al. 2008a). At the mat top, a pH maximum of 8.90 in combination with a pε maximum of $+3.25$ was observed, both values significantly higher than in the water column (pH 8.3; pε $+2.84$). Heterotrophic activity and oxygen consumption then successively decrease pH to near-neutral and pε to very negative values in the pore waters below the mat (Figure 12).

However, detailed microscopy of thin sections shows that oxygenic photosynthetic upper mat parts contain only minor amounts of aragonite precipitates. Specifically, these are aragonite clots which initiate spherulite growth (Figure 8A). These spherulites then become concentrated in the green and purple layer coincident with a decrease in cyanobacterial cells and transition from a homogenously structured to a layered, compacted exopolymer matrix with crevice-like zones (Figures 8A, H). The actual microbialite, with its horizontal layers and vertical sheets, apparently initiates exactly in these crevice-like zones. Here, in the green and purple layer of the microbial mat, pH is around 7.6 (at daylight conditions) and, hence, aragonite supersaturation with intermediate values is expected. Because of that, no exorbitant strong photosynthesis effect, but the degradation of nucleation-inhibiting exopolymers could be the driving mechanism in precipitation.

The resulting microbialite, with its fabric displaying the crevice-like weakness-zones of the exopolymer mat framework, is—with few exceptions—composed of aragonite microspar with thread-like microcrystalline stripes, i.e. is devoid of calcified cyanobacteria or other "calcimicrobe" fossils. Exceptions are conspicuous grey to black horizontal layers with coccoid cyanobacterial remains from Lake 21 and 22 (Figure 13E), and one layer with erect cyanobacterial filament traces from Lake 2. These exceptions indicate that a minor part of the horizontal layers were already formed within cyanobacteria-dominated mats parts, i.e., green or even the orange mat layer, and that aragonite precipitation is not linked to a specific redox zone.

Fibrous aragonite veneers of the microbialite layers and sheets were only found in the microbialite parts below the microbial mat. Here, the carbonates show locally thin, patchy biofilms, but appear to be successively free of a continuous exopolymer cover. Instead, microbes are concentrated in flocculent aggregates within pore spaces. Indeed, gypsum locally nucleates directly upon the carbonate framework. Therefore, a lack of exopolymer films at low but existing supersaturation is considered to permit slow overgrowth of existing carbonate crystals to form fibrous veneers on the microbialite framework.

Stable carbon and oxygen isotope values of microbialites in comparison with marine values, support the interpretation that, after a simultaneous enrichment of ^{18}O and ^{13}C in the lake water by evaporation (indicated by covariation), high photosynthesis and possibly loss of CH_4 to the water column causes very positive δ^{13}C values in the microbial carbonates (Figure 16).

A high depletion of ^{12}C in the organic sedimentary carbon of Kiritimati Lake 30 mats was already noted by Trichet et al. (2001) and was explained by them by a high bioproductivity. Most positive values have been obtained for spherulites and a layer with cyanobacterial filament traces, which are forming in the oxygenic mat parts as the first precipitates. Vertical sheets and horizontal layers, both starting to form in the lowermost green layer and purple layer show similar to significantly less positive δ^{13}C values, thus are consistent with dissolve inorganic carbon derived from degradation of organics combined with moderate photosynthesis. There is no indication of carbonate
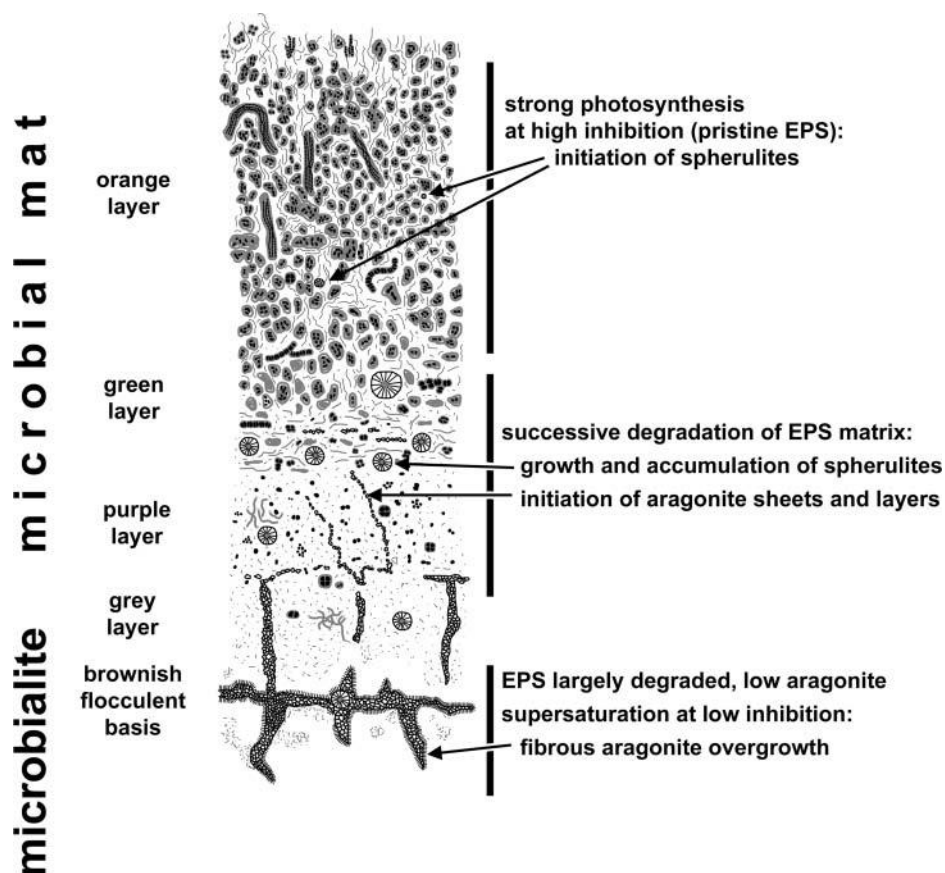
FIG. 17.   Model of microbialite formation in hypersaline lakes on Kiritimati.

precipitation driven by methane consumption. Consequently, on basis of the available information, the following explanation is suggested for the formation of the reticulate microbialites in Kiritimati lakes (Figure 17):

(1) In the orange layer, intensive photosynthesis causes high pH and consequently high supersaturation with respect to aragonite. However, precipitation is efficiently inhibited by pristine exopolymers of the mat layer. At few spots where inhibition is overcome, nucleation and radial aragonite crystal growth starts. Hence, these spherulites are a product of an extraordinary high photosynthesis effect simultaneous to an efficient inhibitory effect by exopolymers.

(2) In deeper parts of the green, and in the purple layer, increasing decarboxylation and hydrolysis of exopolymers cause successive break-down of inhibition. While supersaturation with respect to aragonite is decreased but still high, aragonite crystal nucleation takes place along crevice-like zones of partly degraded exopolymers. Sheet-like aragonite structures with fringed edges form. Hence, reticulate micro-

bialite layers and sheets are a product of high photosynthesis at decreasing inhibition of exopolymers.

(3) Within anoxic porewater below mat, inhibition of aragonite precipitation is almost absent, however, at low supersaturation to saturation. Consequently, slow, syntaxial growth of aragonite crystals at lamellae surfaces occurs. Hence, fibrous aragonite veneers of the microbialite framework are a product of low aragonite supersaturation at almost absence of inhibition.

## DISCUSSION: AUTOTROPHIC VS HETEROTROPHIC PROCESSES IN MICROBIALITE FORMATION

The microbialites of hypersaline lakes on Kiritimati excellently exemplify the common difficulties in identifying a specific microbial process as crucial in microbialite formation. While degradation of inhibiting exopolymers within a photosynthesis-dominated microbial system is favoured as explanation for $CaCO_3$ precipitation and microbialite fabric formation in this paper, a number of other processes with potential effect on carbonate equilibrium and nucleation operate at the same time. Specifically these are, based on the data available, (i) anoxygenic

photosynthesis, (ii) sulfate-reduction, (iii) ammonification, (iv) methanogenesis and methylotrophy. A further question is, why microbialites form in the hypersaline Lakes 2, 21 and 22, but not in the hypersaline Lake 51.

(i) Anoxygenic photosynthetic bacteria (green and purple bacteria) potentially rise the $Ca^{2+} \times CO_3^{2-}$ ion activity product by their assimilation of carbon dioxide:

$$CO_2 + 2H_2S => CH_2O + H_2O + 2S°$$

However, commonly sulfide oxidation further proceeds via elemental sulfur to sulfate, then causing acidification. Moreover, purple non-sulfur bacteria (*Rhodopseudomonas palustris*) have been shown in laboratory experiments to induce $CaCO_3$ precipitation in solutions already supersaturated with respect to $CaCO_3$ minerals (Bosak et al. 2007). Purple non-sulfur bacteria have been shown to be metabolically versatile (Sasikala and Ramana 1998; Larimer et al. 2003), and some of them grow e.g., on methanol (Douthit and Pfennig 1976):

$$2CH_3OH + CO_2 => 3\ CH_2O + H_2O$$
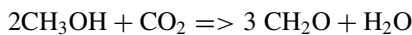
Indeed, purple non-sulfur bacteria clones have been detected in the Kiritimati hypersaline lake microbial mats, and certainly contribute to inorganic carbon fixation. However, based on the currently available data, there is no clear evidence that these microorganisms may play a crucial role in microbialite formation.

(ii) Sulfate-reduction certainly is a significant process in element cycling in Kiritimati hypersaline microbial mats. Sulfide production is evident in lowermost mat parts, and *Deltaproteobacteria* indeed have been detected in brown flocculent aggregates just below the mats (Table 3, Figure 11). In addition, biomarkers detected by Bühring et al. (2009) point to sulfate-reducing bacteria present already in oxic zone of the mats. These may be active in darkness as well as under daylight conditions (Canfield and Des Marais 1991). However, contrary to other metabolic pathways (e.g., oxygenic photosynthesis), the mechanism how sulfate-reducing bacteria affect the carbonate equilibrium is not clear. The sum equation indicates that sulfate-reduction using carbohydrates or organic acids such as acetate increases carbonate alkalinity, which, at constant pH, does only cause a minor rise in CO_3^{2-} activity and hence $CaCO_3$ mineral supersaturation (Aloisi 2008):

$$2\ CH_2O + SO_4^{2-} => H_2S + 2\ HCO_3^-$$
$$CH_3COOH + SO_42- => H_2S + 2\ HCO_3^-$$
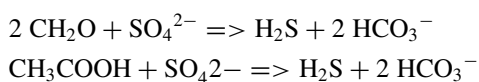
In microbial mats, simultaneous CO_2 release from digestion of organic compounds commonly causes a decrease in pH, and hence decrease in $CaCO_3$ mineral supersaturation. Certainly, the effect of sulfate reduction is dependent on the electron-donor used in the reaction (e.g., H_2 instead of CH_3COOH or CH_2O; Visscher and Stolz 2005). However, if these electron donors are not supplied from an external source but from within the mat, their production from organic precursors is linked with CO_2 liberation, so that the sum effect on the carbonate equilibrium is negligible.

Nonetheless, case studies have demonstrated a spatial correlation of sulfate-reducing bacteria and $CaCO_3$ precipitation (Visscher et al. 2000). However, mechanism of how sulfate-reducing bacteria induced precipitation is currently not fully understood (Baumgartner et al. 2006: 141) and model calculations question the significance of sulfate reduction in inducing $CaCO_3$ precipitation in these mats (Aloisi 2008). One mechanism suggested by Baumgartner et al. (2006) is the modification of the extracellular polymeric substances through partial degradation by bacteria, especially SRB.

However, then, the crucial mechanism is not the process of sulfate-reduction but the exopolymer-digestion by SRB (and other prokaryotes). In any case, detailed studies of exopolymers produced or modified by sulfate-reducing bacteria (Braissant et al. 2007) or other heterotrophic bacteria form a promising field for a clearer understanding of how these microorganisms affect microbialite formation. Apart from that, the effect on the carbonate equilibrium is different, when sulfate-reduction is coupled with other metabolic processes, e.g., Fe^{3+} reduction (Hendry 1993):

$$15\ CH_2O + 2\ Fe_2O_3 + 8\ SO_4^{2-}$$
$$=> 4\ FeS_2 + 15\ HCO_3^- + 7\ H_2O + OH^-$$
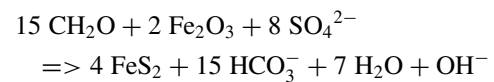
Such coupling might indeed support microbialite formation in settings of sufficient Fe^{3+} supply, e.g., in areas with influx from siliciclastics (e.g., Arp et al. 2008: 1245), or from igneous or metamorphic rocks. However, on the atoll of Kiritimati only carbonate rocks are available for weathering and there is no substantial source of iron (except from former military vehicles). Consequently, iron concentrations in lake and pore waters of Kiritimati lakes are low, and coupling of sulfate reduction with iron reduction is unlikely to occur.

(iii) In contrast, ammonification is substantially involved in the anaerobic decomposition of organic matter in the Kiritimati hypersaline lake microbial mats. This is indicated by high NH_4^+ concentrations in Lake 21 and 22 porewater samples (Table 1). Nonetheless, pH values at the grey mat bottom and within porewaters decrease from 7.6 to 7.16. Thus, the sum effect of all microbial processes including ammonification at the mat basis results in a further decrease in $CaCO_3$ mineral supersaturation. Again, it seems

unlikely that this metabolic process is a crucial factor in microbialite formation in Kiritimati hypersaline lakes.

(iv) The composition of microbial community (Figures 9, 10, 11; Table 3) indicates that methanogenesis as well as methylotrophy may play a significant role in the microbialite-forming mats of Kiritimati hypersaline lakes. For cold seep environments it is known that a combination of sulfate-reduction and methanotrophy fuels the formation of $CaCO_3$ precipitates, which then show significantly ^{13}C-depleted stable isotope values (Roberts et al., 1989). Contrary to this, Kiritimati microbialites show ^{13}C-enriched, positive $\delta^{13}C$ values (Figure 16). No external source of methane (seep) is known, and methane is rather produced within the mats. Here, autotrophic methanogenesis could be important in raising pH by CO_2 consumption (Kenward et al. 2009). The identified methanogens in the investigated mats, however, are methylotrophs, and hence do not consume but release CO_2 only, except when using methylamines:

$$4\ CH_3NH_2 + 2\ H_2O \rightarrow 3\ CH_4 + CO_2 + 4\ NH_3$$
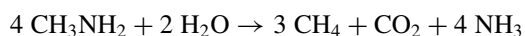
Then, excess of NH_3 release relative to CO_2, and protonation to NH_4^+ increases pH and hence carbonate activity. Indeed, anoxic porewaters in the investigated lakes are high in NH_4^+. However, as discussed with respect to other pathways of ammonification, the observed near neutral pH values in pore spaces below the mat bottom argue against a crucial role of methylamine-consuming methanogens.

Further field and laboratory analysis are required to understand why microbialites form in the hypersaline Lakes 2, 21 and 22, but not in the hypersaline Lake 51. Based on current knowledge, one crucial point that may lead to differences in microbial communities and element cycling might be that Lake 51 receives seawater-recharge via a canal-like connection to lagoon, whereas Lakes 2, 21 and 22 have higher Ca^{2+} concentrations due to additional groundwater and/or surface water influx. In particular, night measurements of physicochemical gradients, and analysis of sulfide and methane concentrations and fluxes, and expression of functional genes (cf. Breitbart et al. 2009), e.g. involved in exopolymer degradation, may contribute to resolve these problems.

CONCLUSIONS

Microbialites with a unique reticulate fabric were discovered below microbial mats in hypersaline lakes on the atoll of Kiritimati. The mats display a clear color-zonation, with an orange top layer, a green, purple and grey layer below, and a brown flocculent basis. Despite of high oxygenic photosynthesis in top parts of the mat and a high aragonite supersaturation in the water column, microbialite formation takes place in lower, oxic to anoxic mat parts. The hypersaline lakes are filled by evaporated seawater modified by $CaCO_3$ and gypsum precipitation. Those

lakes hosting microbialites are in addition enriched in Ca^{2+} via surface and/or subsurface influx.

The prokaryotic community of the microbial mats is characterized by abundant phylotypes closely related to halotolerant taxa and taxa with preference to oligotrophic habitats. Besides *Cyanobacteria*, which are the major primary producers, *Alphaproteobacteria* (among them purple nonsulfur bacteria), *Betaproteobacteria*, *Gammaproteobacteria, Deltaproteobacteria*, *Bacteriodetes*, *Actinobacteria*, *Acidobacteria*, *Spirochaetes*, *Firmicutes*, *Chloroflexi*, *Planctomycetes*, *Crenarchaeota*, *Euryarchaeota*, representatives of the candidate phyla TM6 and OP8, as well as unclassified taxa were detected.

Complementary to the methylotrophic genus *Methanohalophilus*, which is likely a dominant methanogen in the basal mat parts, a number of phylotypes throughout the different mat layers parts find their closest known relatives in representatives from methane seep environments. This points to a significant cycling of methane and methyl compounds within the mats. Indeed, stable isotope analyzes point to carbonate precipitation from an inorganic carbon pool depleted in ^{12}C, due to photosynthesis and/or methanogenesis.

The microbialite consist of three aragonitic structural components: spherulites, layers and sheets, and fibrous veneers. Spherulites start forming already in orange top parts of the mat, are thus interpreted as a result of extraordinary high photosynthesis overcoming inhibition by pristine exopolymers. Microbial layers and sheets start forming in crevice-like zones of green and purple mat parts, where photosynthesis is still active. Consequently, break-down of exopolymers inhibiting precipitation concurrent to photosynthetic carbon assimilation is considered as key factor in microbialite formation.

The final fibrous aragonite veneers may reflect slow syntaxial overgrowth at low supersaturation and almost lack of inhibiting exopolymers. While sulfate reduction, methylotrophy, methanogenesis and ammonification play an important role in element cycling of the mat, there is currently no evidence for a crucial role in the formation of microbialite in the hypersaline lakes of Kiritimati.

REFERENCES

Aloisi G. 2008. The calcium carbonate saturation state in cyanobacterial mats throughout Earth's history. Geochim Cosmochim Acta 72:6037–6060.

Aloisi G, Bouloubassi I, Heijs SK, Pancost RD, Pierre C, Sinninghe Damsté JS, Gottschal JC, Forney LJ, Rouchy JM. 2002. CH_4-consuming microorganisms and the formation of carbonate crusts at cold seeps. Earth Planet Sci Lett 203:195–203.

Altschul SF, Madden TL, Schäffer AA, Zhang J, Zhang Z, Miller W, Lipman DJ. 1997. Gapped BLAST and PSI-BLAST: a new generation of protein database search programs. Nucl Acids Res 25:3389–3402.

Anandham R, Indiragandhi P, Madhaiyan M, Chung J, Ryu KY, Jee HJ & Sa T. 2009. Thiosulfate oxidation and mixotrophic growth of *Methylobacterium goesingense* and *Methylobacterium fujisawaense*. J Microbiol Biotechnol 19:17–22.

Arp G, Bissett A, Brinkmann N, Cousin S, de Beer D, Friedl T, Mohr KI, Neu TR, Reimer A, Shiraishi F, Stackebrandt E, Zippel B. 2010. Tufa-forming

biofilms of German karstwater streams: Microorganisms, exopolymers, hydrochemistry and calcification. Geol Soc Spec Publ 336:83–118.

Arp G, Hofmann J, Reitner J. 1998. Microbial fabric formation in spring mounds ("Microbialites") of alkaline salt lakes in the Badain Jaran Sand Sea, PR China. Palaios 13:581–592.

Arp G, Reimer A, Reitner J. 2001. Photosynthesis-induced biofilm calcification and calcium concentrations in Phanerozoic oceans. Science 292:1701–1704.

Arp G, Thiel V, Reimer A, Michaelis W, Reitner J. 1999. Biofilm exopolymers control microbialite formation at thermal springs discharging into the alkaline Pyramid Lake, Nevada, USA. Sediment Geol 126:159–176.

Baumgartner LK, Reid RP, Dupraz C, Decho AW, Buckley DH, Spear JR, Przekop KM, Visscher PT. 2006. Sulfate reducing bacteria in microbial mats: changing paradigms, new discoveries. Sediment Geol 185:131–145.

Bissett A, de Beer D, Schoon R, Shiraishi F, Reimer A, Arp G. 2008. Microbial mediation of stromatolite formation in karst-water creeks. Limnol Oceanogr 53:1159–1168.

Bosak T, Greene SE, Newmann DK. 2007. A likely role for anoxygenic photosynthetic microbes in the formation of ancient stromatolites. Geobiology 5:119–126.

Braissant O, Decho AW, Dupraz C, Glunk C, Przekop KM, Visscher PT. 2007. Exopolymeric substances of sulfate-reducing bacteria: Interactions with calcium at alkaline pH and implication for formation of carbonate minerals. Geobiology 5:401–411.

Breitbart M, Hoare A, Nitti A, Siefert J, Haynes M, Dinsdale E, Edwards R, Souza V, Rohwer F, Hollander D. 2009. Metagenomic and stable isotopic analyzes of modern freshwater microbialites in Cuatro Ciénegas, Mexico. Environ Microbiol 11:16–34.

Bühring SI, Smittenberg RH, Sachse D, Lipp JS, Golubić S, Sachs JP, Hinrichs KU, Summons RR. 2009. A hypersaline microbial mat from the Pacific Atoll Kiritimati: insights into composition and carbon fixation using biomarker analyzes and a ^{13}C-labeling approach. Geobiology 7:1–16.

Canfield DE, Des Marais DJ. 1991. Aerobic sulfate reduction in microbial mats. Science 251: 1471–1473.

Cavicchioli R, Fegatella F, Ostrowski M, Eguchi M, Gottschal J. 1999. Sphingomonads from marine environments. J Indust Microbiol Biotechnol 23:268–272.

Cole JR, Chai B, Marsh TL, Farris RJ, Wang Q, Kulam SA, Chandra S, McGarrell DM, Schmidt TM, Garrity GM, Tiedje JM. 2003. The Ribosomal Database Project (RDP-II): previewing a new autoaligner that allows regular updates and the new prokaryotic taxonomy. Nucl Acids Res 31:442–443.

Davidova IA, Harmsen HJM, Stams AJM, Belyaev SS, Zehnder AJB. 1997. Taxonomic description of *Methanococcoides euhalobius* and its transfer to the *Methanohalophilus* genus. Anton van Leeuw 71:313–318.

Défarge C, Trichet J, Jaunet AM, Robert M, Tribble J, Sansone F. 1996. Texture of microbial sediments revealed by cryo-scanning electron microscopy. J Sediment Res 66:935–947.

Denger K, Stackebrandt E, Cook AM. 1999. *Desulfonispora thiosulfatigenes* gen. nov., sp. nov., a taurine-fermenting, thiosulfate-producing anaerobic bacterium. Inter J Syst Bacteriol 49:1599–1603.

Dotzauer C, Ehrmann MA, Vogel RF. 2002. *Thermoanaerobacterium* and *Thermoanaerobacter* in canned food. Food Technol Biotechnol 40:21–26.

Douthit HA, Pfennig N. 1976. Isolation and growth rates of methanol utilizing Rhodospirillaceae. Arch Microbiol 107:233–234.

Dupraz C, Reid RP, Braissant O, Decho AW, Norman RS, Visscher PT. 2009. Processes of carbonate precipitation in modern microbial mats. Earth-Sci Rev 96:141–162.

Dupraz CD, Visscher PT, Baumgartner LK, Reid RP. 2004. Microbe-mineral interactions: early carbonate precipitation in a hypersaline lake (Eleuthera Island, Bahamas). Sedimentology 51:745–765.

Fahy A, Ball AS, Lethbridge G, Timmis KN, McGenity TJ. 2008. Isolation of alkali-tolerant benzene-degrading bacteria from a contaminated aquifer. Lett Appl Microbiol 47:60–66.

Falkland AC, Woodroffe CD. 1997. Geology and hydrogeology of Tarawa and Kiritimati, Kiribati. Develop Sedimentol 54:577–610.

Garrett P. 1970. Phanerozoic stromatolites: noncompetitive ecologic restriction by grazing and burrowing animals. Science 169:171–173.

Gleave AP, Taylor RK, Morris BA, Greenwood DR. 1995. Cloning and sequencing of a gene encoding the 69-kDa extracellular chitinase of *Janthinobacterium lividum*. FEMS Microbiol Lett 131:279–288.

Government of Kiribati. 1993. Republic of Kiribati 1:50,000, Sheet Kiritimati (Christmas Island). Series X782 (DOS 436) Edition 8-OS 1993, Ordnance Survey.

Green PN. 2006. *Methylobacterium*. In: Dworkin M, Falkow S, Rosenberg E, Schleifer KH, Stackebrandt E, editors. The Prokaryotes, Volume 5: Proteobacteria: Alpha and Beta Subclasses. New York: Springer. P 257–265.

Hendry JP. 1993. Calcite cementation during bacterial manganese, iron and sulphate reduction in Jurassic shallow marine carbonates. Sedimentology 40:87–106.

Huber T, Faulkner G, Hugenholtz P. 2004. Bellerophon; a program to detect chimeric sequences in multiple sequence alignments. Bioinformatics 20:2317–2319.

Huber JA, Johnson HP, Butterfield DA, Baross JA. 2006. Microbial life in ridge flank crustal fluids. Environ Microbiol 8:88–99.

Isenbarger TA, Finney M, Rios-Velazquez C, Handelsman J, Ruvkun G. 2008. Miniprimer PCR, a new lens for viewing the microbial world. Appl Environ Microbiol 74:840–849.

Jones B, Renaut RW. 1996. Morphology and growth of aragonite crystals in hot-spring travertines at Lake Bogoria, Kenya Rift Valley. Sedimentology 43:323–340.

Kahle CF. 1994. Facies and evolution of Silurian coral-microbialite reef complex, Maumee, Ohio, USA. J Sediment Res 64a:711–725.

Kempe S, Kazmierczak J. 1990. Calcium carbonate supersaturation and the formation of in situ calcified stromatolites. In: Ittekkot VA, Kempe S, Michaelis W, Spitzy A, editors. Facets of Modern Biogeochemistry. Berlin: Springer. P 255–278.

Kempe S, Kazmierczak J, Landmann G, Konuk T, Reimer A, Lipp A. 1991. Largest known microbialites discovered in Lake Van, Turkey. Nature 349:605–608.

Kenward PA, Goldstein RH, González LA, Roberts JA. 2009. Precipitation of low-temperature dolomite from an anaerobic microbial consortium: the role of methanogenic Archaea. Geobiology 7:556–565.

Knittel K, Boetius A, Lemke A, Eilers H, Lochte K, Pfannkuche O, Linke P, Amann R. 2003. Activity, distribution, and diversity of sulfate reducers and other bacteria in sediments above gas hydrate (Cascadia Margin, Oregon). Geomicrobiol J 20:269–294.

Komárek J, Anagnostidis K. 1999. Cyanoprokaryota, Teil 1. Chroococcales. In: Ettl H, Gerloff J, Heynig H, Mollenhauer D, editors. Süßwasserflora von Mitteleuropa. Heidelberg: Spektrum. Band 19/1. 548 pp.

Lane DJ. 1991. 16S/23S rRNA sequencing. In: Stackebrandt E, Godfellow M, editors. Nucleic Acid Techniques in Bacterial Systematics. New York, NY: John Wiley and Sons. P 115–175.

Lanoil BD, Sassen R, La Duc MT, Sweet ST, Nealson KH. 2001. Bacteria and Archaea physically associated with Gulf of Mexico gas hydrates. Appl Environ Microbiol 67:5143–5153.

Larimer FW, Chain P, Hauser L, Lamerdin J, Malfatti S, Do L, Land ML, Pelletier DA, Beatty JT, Lang AS, Tabita FR, Gibson JL, Hanson TE, Bobst C, Torres y Torres JL, Peres C, Harrison FH, Gibson J, Harwood CS. 2003. Complete genome sequence of the metabolically versatile photosynthetic bacterium *Rhodopseudomonas palustris*. Nature Biotechnol 22:55–61.

Laval B, Cady SL, Pollack JC, McKay CP, Bird JS, Grotzinger JP, Ford DC, Bohm HR. 2002. Modern freshwater microbialite analogues for ancient dendritic reef structures. Nature 407:626–629.

Lenke H, Pieper DH, Bruhn C, Knackmuss HJ. 1992. Degradation of 2,4-Dinitrophenol by two *Rhodococcus erythropolis* strains, HL 24-1 and HL 24-2. Appl Environ Microbiol 58:2928–2932.

Lim DSS, Laval BE, Slater G, Antoniades D, Forrest AL, Pike W, Pieters R, Saffari M, Reid D, Schulze-Makuch D, Andersen D, McKay CP. 2009. Limnology of Pavilion Lake, B. C., Canada—Characterization of a microbialite forming environment. Fundam Appl Limnol 173:329–351.

Liu Y, Boone DR, Choy C. 1990. *Methanohalophilus oregonense* sp. nov. a methylotrophic methanogen from an alkaline, saline aquifer. Inter J System Bacteriol 40:111–116.

Lloyd KG, Lapham L, Teske A. 2006. An anaerobic methane-oxidizing community of ANME-1b Archaea in hypersaline Gulf of Mexico sediments. Appl Environ Microbiol 72:7218–7230.

Minz D, Fishbain S, Green SJ, Muyzer G, Cohen Y, Rittmann BE, Stahl D. 1999. Unexpected population distribution in a microbial mat community: Sulfate-reducing bacteria localized to the highly oxic chemocline in contrast to a eukaryotic preference for anoxia. Appl Environ Microbiol 65:4659–4665.

Northrop J. 1962. Geophysical observations on Christmas Island. Atoll Research Bulletin 89:1–2.

Orphan VJ, Hinrichs KU, Ussler W III, Paull CK, Taylor LT, Sylva SP, Hayes JM, DeLong EF. 2001. Comparative analysis of methane-oxidizing archaea and sulfate-reducing bacteria in anoxic marine sediments. Appl Environ Microbiol 67:1922–1934.

Orphan VJ, Jahnke LL, Embaye T, Turk KA, Pernthaler A, Summons RE, Des Marais DJ. 2008. Characterization and spatial distribution of methanogens and methanogenic biosignatures in hypersaline microbial mats of Baja California. Geobiology 6:376–393.

Palleroni NJ. 2005. Genus I. *Burkholderia*. In: Garrity GM, editor. Bergey's manual of systematic bacteriology. 2nd ed. Volume 2 The Proteobacteria Part C The Alpha-, Beta-, Delta-, and Epsilonproteobacteria. New York: Springer. P 575–600.

Parcell WC. 2002. Sequence stratigraphic controls on the development of microbial fabrics and growth forms-implications for reservoir quality distribution in the Upper Jurassic (Oxfordian) Smackover Formation, eastern Gulf Coast, USA. Carbonates and Evaporites 17:166–181.

Parkhurst DL, Appelo CAJ. 1999. User's guide to PHREEQC (version 2)- a computer program for speciation, batch-reaction, one-dimensional transport, and inverse geochemical calculations. U.S. Geological Survey Water-Resources Investigations Report 99-4259:1–312.

Pascual J, Macián MC, Arahal DR, Garay E, Pujalte MJ. 2010. Multilocus sequence analysis of the central clade of the genus *Vibrio* by using the 16S rRNA, recA, pyrH, rpoD, gyrB, rctB and toxR genes. Inter J System Evolution Microbiol 60:154–165.

Paterek JR, Smith PH. 1988. *Methanohalophilus mahii* gen. nov., sp. nov., a methylotrophic halophilic methanogen. Inter J System Bacteriol 38:122–123.

Pentecost A. 2005. Travertine. Berlin: Springer. 445 p.

Peters F, Rother M, Boll M. 2004. Selenocysteine-containing proteins in anaerobic benzoate metabolism of *Desulfococcus multivorans*. J Bacteriol 186:2156–2163.

Pratt BR. 1982. Stromatolitic framework of carbonate mud-mounds. J Sediment Petrol 52:1203–1227.

Purdy EG, Gischler E. 2005. The transient nature of the empty bucket model of reef sedimentation. Sediment Geol 175:35–47.

Reid RP, Browne KM. 1991. Intertidal stromatolites in a fringing Holocene reef complex, Bahamas. Geology 19:15–18.

Richert L, Golubić S, Le Guédès R, Hervé A, Payri C. 2006. Cyanobacterial populations that build 'kopara' microbial mats in Rangiroa, Tuamotu Archipelago, French Polynesia. Euro J Phycol 41:259–279.

Riding R. 2000. Microbial carbonates: the geological record of calcified bacterial-algal mats and biofilms. Sedimentology 47 (Supplement 1):179–214.

Risatti JB, Capman WC, Stahl DA. 1994. Community structure of a microbial mat: the phylogenetic dimension. Proc Natl Acad Sci USA 91:10173–10177.

Roberts HH, Sassen R, Carney R, Aharon P. 1989. ^{13}C-depleted authigenic carbonate buildups from hydrocarbon seeps, Louisiana continental slope. Gulf Coast Asso Geol Soc Trans 39:523–530.

Robertson CE, Spear JR, Harris JK, Pace NR. 2009. Diversity and stratification of archaea in a hypersaline microbial mat. Appl Environ Microbiol 75:1801–1810.

Sachse D, Sachs JP. 2008. Inverse relationship between D/H fractionation in cyanobacterial lipids and salinity in Christmas Island saline ponds. Geochim et Cosmochim Acta 72:793–806.

Saenger C, Miller M, Smittenberg RH, Sachs JP. 2006. A physico-chemical survey of inland lakes and saline ponds: Christmas Island (Kiritimati) and Washington (Teraina) Islands, Republic of Kiribati. Saline Systems 2006, 2:8. doi: 10.1186/1746-1448-2-8.

Sambrook J, Russell DW. 2001. Molecular Cloning—A Laboratory Manual. 3rd ed., Cold Spring Harbor: Cold Spring Harbor Laboratory Press. 2344 p.

Sasikala C, Ramana CV. 1998. Biodegradation and metabolism of unusual carbon compounds by anoxygenic phototrophic bacteria. Advan Microb Physiol 39: 339–377.

Shiraishi F, Bissett A, de Beer D, Reimer A, Arp G. 2008a. Photosynthesis, respiration and exopolymer calcium-binding in biofilm calcification (Westerhöfer and Deinschwanger Creek, Germany). Geomicrobiol J 25:83–94.

Shiraishi F, Zippel B, Neu TR, Arp G. 2008b. In situ detection of bacteria in calcified biofilms using FISH and CARD–FISH. J Microbiol Meth 75:103–108.

Stahl DA, Key R, Flesher B, Smit J. 1992. The phylogeny of marine and freshwater Caulobacters reflects their habitat. J Bacteriol 174:2193–2198.

Staley JT, Konopka AE, Dalmasso JP. 1987. Spatial and temporal distribution of *Caulobacter* spp. in two mesotrophic lakes. FEMS Microbiol Ecol 45:1–6.

Tamura K, Dudley J, Nei M, Kumar S. 2007. MEGA 4: Molecular Evolutionary Genetics Analysis (MEGA) software version 4.0. Mol Biol Evol 24:1596–1599.

Trichet J, Défarge C, Tribble J, Tribble G, Sansone F. 2001. Christmas Island lagoonal lakes, models for the deposition of carbonate—evaporite—organic laminated sediments. Sediment Geol 140:177–189.

Valencia M. 1977. Christmas Island (Pacific Ocean): reconnaissance geologic observations. Atoll Res Bull 197:1–14.

Van Aken B, Peres CM, Doty SL, Yoon JM, Schnoor JL. 2004. *Methylobacterium populi* sp. nov., a novel aerobic, pink-pigmented, facultatively methylotrophic, methane-utilizing bacterium isolated from poplar trees (*Populus deltoidesxnigra* DN34). Inter J Syst Evol Microbiol 54:1191–1196.

Visscher PT, Reid RP, Bebout BM. 2000. Microscale observations of sulfate reduction: correlation of microbial activity with lithified micritic laminae in modern marine stromatolites. Geology 28:919–922.

Visscher PT, Stolz JF. 2005. Microbial mats as bioreactors: populations, processes, and products. Palaeogeogr Palaeoclimatol Palaeoecol 219:87–100.

von Pia J. 1934. Die Kalkbildung durch Pflanzen. Beihefte zum botanischen Zentralblatt A 52:1–72.

Widdel F. 1980. Anaerober Abbau von Fettsäuren und Benzoesäure durch neu isolierte Arten. Ph.D. thesis, University of Göttingen, Göttingen. 443 p.

Winderl C, Anneser B, Griebler C, Meckenstock RU, Lueders T. 2008. Depth-resolved quantification of anaerobic toluene degraders and aquifer microbial community patterns in distinct redox zones of a tar oil contaminant plume. Appl Environ Microbiol 74:792–801.

Winsborough BM, Seeler JS, Golubic S, Folk RL, Maguire B Jr. 1994. Recent fresh-water lacustrine stromatolites, stromatolitic mats and oncoids from Northeastern Mexico. In: Bertrand-Sarfati J., Monty C. editors. Phanerozoic stromatolites II. Dordrecht: Kluwer. P 71–100.

Woodroffe CD, McLean RF. 1998. Pleistocene morphology and Holocene emergence of Christmas (Kiritimati) Island, Pacific Ocean. Coral Reefs 17:235–248.